North Pacific response to hemispheric warming forces Holocene drought

Victoria Todd (victoriatodd@utexas.edu)
University of Texas at Austin https://orcid.org/0000-0001-5510-2563
Timothy Shanahan
University of Texas at Austin
Pedro DiNezio
University of Colorado
Jeremy Klavans
University of Colorado
Peter Fawcett
Department of Earth and Planetary
R. Scott Anderson
Northern Arizona University
Gonzalo Jimenez-Moreno
Universidad de Granada https://orcid.org/0000-0001-7185-8686
Allegra LeGrande
NASA Goddard Institute for Space Studies
Francesco Pausata
University of Quebec in Montreal https://orcid.org/0000-0001-5182-8420
Alex Thompson
Washington University in St. Louis https://orcid.org/0000-0002-8037-5990
Jiang Zhu
National Center for Atmospheric Research https://orcid.org/0000-0002-0908-5130

Physical Sciences - Article

Keywords:

Posted Date: September 22nd, 2023

DOI: https://doi.org/10.21203/rs.3.rs-3317761/v1

Additional Declarations: There is **NO** Competing Interest.

North Pacific response to hemispheric warming forces Holocene drought

Authors: Victoria L. Todd*[1], Timothy M. Shanahan[1], Pedro N. DiNezio[2], Jeremy M. Klavans[2], Peter J. Fawcett[3], R. Scott Anderson[4], Gonzalo Jiménez-Moreno[5], Allegra N. LeGrande[6,7], Francesco S.R. Pausata[8], Alexander J. Thompson[9], Jiang Zhu[10]

*Corresponding author: victoriatodd@utexas.edu

Affiliations:
[1]Jackson School of Geosciences, The University of Texas at Austin
[2] Department of Atmospheric and Oceanic Sciences, The University of Colorado-Boulder
[3]The Department of Earth and Planetary Sciences, The University of New Mexico
[4]School of Earth and Sustainability, Northern Arizona University
[5]Departamento de Estratigrafía y Paleontología, Universidad de Granada, 18002, Granada, Spain
[6]Center for Climate Systems Research, Columbia University, New York, NY, USA
[7]NASA Goddard Institute for Space Studies, New York, NY, USA
[8]Centre ESCER and GEOTOP, Department of Earth and Atmospheric Sciences, University of Quebec in Montreal, Montreal, QC, Canada
[9]Department of Earth and Planetary Sciences, Washington University, St. Louis
[10]Climate and Global Dynamics Laboratory, National Center for Atmospheric Research, Boulder, CO

Summary:
The Southwest United States is prone to severe and persistent drought[1], but the influence of anthropogenic forcing on current and future precipitation remains uncertain[2-7]. To improve our understanding of the drivers of Southwest drought, we quantified precipitation and temperature changes in the southern Rockies and combined these with a multi-model ensemble of climate simulations for the mid-Holocene, a past interval when the region experienced exceptional and persistent drought. Reconstructed mid-Holocene warming in the Rockies is consistent with existing proxy reconstructions. In most models, this warming only occurs in simulations with prescribed mid-Holocene vegetation, including a "greening" of the Sahara, supporting the hypothesis that expanded vegetation was critical for producing warming consistent with proxy data[15]. In response to this hemispheric warming, a distinct pattern of higher temperatures resembling the negative phase of the Pacific Decadal Oscillation emerges in the models, increasing the magnitude of wintertime precipitation declines across the western US, in better agreement with proxy reconstructions. A similar forced response could be excited by anthropogenic forcings, enhancing future drought across the Southwest US. However, reductions in winter precipitation associated with the development of this pattern of North Pacific warming are underestimated in simulations of both the mid-Holocene and the instrumental period, suggesting that current projections may underestimate the magnitude and the risk of persistent human-made drought in the future.

Main text:
The Southwest United States has experienced an increase in the frequency and severity of droughts over the last century, with the past two decades identified as the worst megadrought in the past 1200 years[1]. However, the magnitude of the human influence on current and future

precipitation is not well constrained, mainly because it is unclear how atmospheric circulation patterns respond to warmer temperatures (e.g., ref.[2]). This is the case for the current megadrought, which has been attributed to a combination of anthropogenic and natural drivers. For example, current rainfall deficits have been attributed mainly to changes in atmospheric dynamics associated with naturally occurring modes of variability affecting the delivery of moisture by wintertime storms[3-7]. And though thermodynamic effects, such as atmospheric evaporative demand[8], have a more discernible human influence, their impact remains small relative to non-anthropogenic changes in circulation[2,9].

Paleoclimate archives can provide insights into the causes of past and future droughts by allowing us to investigate how the climate system responds to external forcings. For example, during the mid-Holocene (6 ka), the Southwest US experienced widespread and prolonged aridity in response to changes in solar insolation[10-12]. Proxy data syntheses and climate model simulations indicate that mid-Holocene drying could have been driven by shifts in the position of the winter storm track directly forced by summer insolation-driven changes in high latitude temperature and a weakening of the equator-to-pole temperature gradient[10-14]. However, they disagree on the magnitude of Northern Hemisphere warming and precipitation changes over the Southwest US[15]. Furthermore, the spatial pattern of the rainfall changes in the western US is poorly known, hindering our understanding of the mechanisms driving these changes. Insolation-driven strengthening of summer monsoon systems in the early to mid-Holocene[13,16,17] also complicates the attribution of hydroclimatic changes in proxy records from the Southwest US, because they often reflect the combined influence of winter and summer precipitation. Together, these issues have made our understanding of the magnitude, spatial extent, and causes of drought in this water-dependent area of the US less certain.

To study the mechanisms of forced drought in the western US, we generated two Holocene records of hydrologic variability in the southern Rocky Mountains, in the core of the region currently experiencing drought. Our sites, Stewart Bog (SB) in the Sangre de Cristo Mountains of northern New Mexico and Hunters Lake (HL) in the San Juan mountains of southern Colorado (Extended Data Fig. 1), are well located to capture changes in the southern edge of the Northern Hemisphere storm track[18] while also being at the northernmost extent of the North American Monsoon[16,19]. We quantified past changes in temperature and precipitation using the MBT'$_{5ME}$ index and the hydrogen isotope composition of sedimentary leaf waxes (δD_{wax}), respectively. MBT'$_{5ME}$ temperatures were computed using the BayMBT calibration[20,21] and a compilation of modern empirical calibration samples that includes mid-latitude sites most appropriate for our study locations (Methods). We interpret δD_{wax} as a record of past changes in the stable isotopic composition of precipitation[22], which in this region is controlled by the relative proportions of seasonal moisture sources[23]. At both sites, average winter precipitation stable isotope values are significantly more negative (δD_{SB}: -116±10‰, δD_{HL}: -153±5‰) than the values for summer monsoon precipitation[23,24] (δD_{SB}: -56±8‰, δD_{HL}: -60±5‰) (Extended Data Fig. 1), and available data suggest little influence of an isotope amount effect on precipitation[12,25]. As a result, we interpret the leaf wax isotope signatures preserved in our sites as reflecting changes in the relative proportions of winter and summer moisture sources and estimate past changes in seasonal contributions using a Bayesian isotope mixing model (Methods).

To understand the drivers of mid-Holocene drought in North America, we investigated the climate response in 23 different climate model simulations (Extended Data Table 1) performed under 6 ka boundary conditions and compared these results against new syntheses of proxy data from across western North America. Although our records show that the most extreme drought may have occurred slightly earlier, we focus on 6 ka because of the large number of available simulations. The ensemble includes 13 simulations conducted as part of phase 3 of the Paleoclimate Modeling Intercomparison Project (PMIP3), forced with mid-Holocene insolation and greenhouse gases[26]. We complement these simulations with ten mid-Holocene simulations with prescribed changes in vegetation cover over northern Africa (Green Sahara) or both northern Africa and Siberia – areas with well-established palaeoecological evidence for expanded vegetation during the early and mid-Holocene. Two of the PMIP3 simulations in the ensemble incorporated dynamic vegetation changes, which display more limited vegetation changes than the prescribed runs, providing an intermediate case for evaluating the influence of vegetation on climate. To assess the proxy-model agreement, we generated new syntheses of proxy sea surface temperature data from the North Pacific and proxy hydroclimate records from the western US, drawing from existing compilations and the published literature (Methods; Extended Data Table 2).

The leaf wax isotope records from Hunters Lake and Stewart Bog reveal substantial, coherent shifts in winter precipitation delivered to the southernmost Rockies during the late glacial and Holocene periods (Fig.1). High proportions of winter precipitation at the base of the records, indicated by more negative δD values, undergo a positive isotopic shift at ca. 11.7 ka, reflecting the onset of early to mid-Holocene winter drought. At both sites, positive isotopic values indicate winter drought conditions continued until ca. 5.5 ka, albeit with a brief return to more negative isotope values between ~8.5-6.5 ka, before gradually ameliorating to near modern conditions in the late Holocene (~4 ka). The pattern and timing of the changes in the leaf wax records from the southern Rockies are remarkably consistent with those in a published speleothem isotope record from southern Nevada[12], indicating a large-scale, coherent pattern of hydroclimatic changes across western North America during the mid-Holocene. There are also coherent spatial patterns in the magnitudes of the isotope anomalies. The isotopic anomaly ca. 9 ka is similar at Hunters Lake and Leviathan Cave, both of which are situated to the west ($\Delta\delta D_{Hunters}$ = ca. 20‰ and $\Delta\delta D_{Leviathan}$=24‰; converted from $\delta^{18}O$). The mid-Holocene isotope anomaly is nearly twice as large ($\Delta\delta D$ = 47‰) at Stewart Bog, which is located to the south and east of these sites. This suggests that either the drought at Stewart Bog was more severe, perhaps because of its more southerly location, or that the mid-Holocene drought was characterized by spatially variable differences in the magnitudes of the changes in seasonal moisture sources.

MBT'$_{5ME}$ reconstructed temperatures from Stewart Bog and Hunters Lake indicate a mid-Holocene thermal maximum at ca.10.5 ka, 0.9°C to 0.5°C warmer than present, respectively. The magnitude and timing of Holocene temperature changes are broadly consistent with the evidence for warming in existing Northern Hemisphere temperature syntheses[27-28] (~0.78±0.3ºC). Proxy evidence for early Holocene warming has been disputed based on climate model simulations, which do not show warming in response to stronger summer insolation (i.e., the "Holocene temperature conundrum"). However, a recent study demonstrated that the inclusion of prescribed Northern Hemisphere vegetation changes, particularly over north Africa (i.e., "Green Sahara"[15]), can produce substantial (~0.89°C) mean annual warming of the Northern Hemisphere (30 to

90ºN) in mid-Holocene simulations, consistent with proxy reconstructions[27-28]. The results of our multi-model comparison, in which each mid-Holocene simulation was run with fixed preindustrial vegetation, prescribed "Green Sahara" vegetation, and (in two models) prescribed "Green Sahara" and expanded Arctic and mid-latitude vegetation, show that the warming effect is robust across different models- though the magnitude of the changes varies (0.35 to 1.2°C).

To constrain the magnitude of mid-Holocene drought at our study sites, we developed a Bayesian mixing model that estimates the relative proportions of summer and winter rainfall responsible for the observed increases in leaf wax isotope values (Methods). We assumed that annual precipitation during the mid-Holocene was less than during the preindustrial based on ubiquitous proxy evidence for drying between 8.5 and 4 ka[29-31]. Our Bayesian model indicates that substantial reductions in winter precipitation are required to achieve the observed leaf wax isotopic signatures for the mid-Holocene (Fig. 2a). We estimate minimum decreases in winter moisture of 20% (SB) to 17% (HL), though the declines could be much larger, depending on changes in summer precipitation. For example, these minimum estimates for winter precipitation changes require substantial increases in summer precipitation (SB: 17-28%, HL: 11-18% (3σ)). Published seasonal precipitation reconstructions from pollen at our study sites suggest that changes in monsoon precipitation at these locations were small[16]. If monsoon precipitation did not increase at these sites, then the magnitudes of winter moisture decrease required to explain the leaf wax records are much larger (SB: >33%, HL: >24%). However, these estimates of winter precipitation deficits are consistent with published estimates from pollen reconstructions[11] (11-29%) and paleo lake level modeling[32] (<40%).

The majority of models simulate reductions in winter precipitation during the mid-Holocene, though the magnitudes of these changes are smaller than estimated from our proxy data (Extended Data Table 1). In the PMIP3 models, winter rainfall reductions averaged over the Southwest do not exceed 11% across all models, with overall reductions at our proxy sites that are less than ~70% of what the isotopic data suggest, even assuming large (11-28%) increases in summer monsoon rainfall (Fig.2). One factor that may be responsible for this model-data discrepancy is that the PMIP3 models also underestimate the magnitude of mid-Holocene warming, which may impact precipitation through direct thermodynamic forcing or through the effect of a weaker temperature gradient on the storm tracks[33]. The impact of temperature on winter precipitation is evident in the PMIP3 models (excluding bcc-csm1-1), which exhibit a statistically significant correlation between the magnitude of the simulated decrease in winter precipitation at both sites and warming over the Northern Hemisphere (Fig. 2a,c, SB: $R^2 = 0.396$, $p < 0.038$, HL: $R^2 = 0.317$, $p < 0.07$).

A similar temperature dependent reduction in winter moisture is also evident in the models with prescribed vegetation. While simulated mid-Holocene precipitation changes vary widely amongst the models, the additional warming induces significant additional reductions in winter precipitation over the Southwest US in all the models. An exception is the EC-Earth model, which shows relatively large warming (0.9°C) yet little reduction in winter precipitation (1.4%). This appears to be because the model is already exceptionally sensitive to insolation forcing, showing a temperature (1.4°C) and winter drought response (-5%) comparable to the response in other models with prescribed vegetation. As a result, expanded vegetation in the EC-Earth model produces comparatively small additional changes in temperature and precipitation.

This observation is important as it shows that hemispheric warming is responsible for the wintertime precipitation response in the Southwest US and that multiple factors, such as insolation or vegetation, can produce drought as long as they drive pronounced Northern Hemisphere warming.

Our simulations show that wintertime precipitation deficits are not simply a consequence of changing meridional temperature gradients, as suggested previously[11], and instead result from a coupled ocean-atmosphere response centered in the Pacific Ocean. Enhanced hemispheric warming produces a distinct pattern of sea-surface temperature change over the North Pacific, with intense surface warming extending across the mid to high-latitude western Pacific surrounded by a "horseshoe" pattern of minimal surface warming or cooling to the east (Fig. 3d) and a weaker La Niña-like pattern in the tropical Pacific. These ocean temperature patterns are accompanied by a region of increased sea level pressure over the North Pacific, a response that is consistent with a weakened Aleutian Low (Fig. 3b). This distinct surface temperature and pressure pattern is reminiscent of the negative phase of the Pacific Decadal Oscillation (PDO), which has been implicated in the length and severity of recent wintertime drought over the southwestern US[3-7]. Simulations without vegetation-driven hemispheric warming do not show this PDO-like response and instead cool over most of the North Pacific with a muted atmospheric response, as reported previously[14]. Although it has been previously argued that the observed PDO arises naturally driven by stochastic processes in the ocean-atmosphere system[34], our results suggest that a similar pattern may be excited by hemispheric warming, whether due to vegetation feedbacks or other hemispheric forcings.

Support for a negative PDO-like response comes from our synthesis of Pacific sea-surface temperatures (SSTs). Proxy records show changes in SST that are significantly correlated with the simulated PDO-like pattern in the simulations with expanded vegetation and hemispheric warming (Fig. 3e). Proxy-inferred SST changes in key regions over the North Pacific support a PDO-like pattern despite their limited spatial coverage, particularly away from the coastlines. Marine records off the coast of Japan show localized warming (>2°C) that is most consistent with a PDO-like pattern. Proxy SST data from coastal California display cooling indicative of stronger coastal upwelling, consistent with a weakening of the Aleutian Low. In the simulations, the development of a negative PDO-like pattern occurs in response to the advection of warmer continental air over the North Pacific by the westerly winds and, to a lesser extent, by the global response to the radiative effect of reduced dust emissions from Africa and Siberia (Extended Data Fig. 6). Both occur due to the local and remote effects of vegetation changes on albedo and are amplified by reduced sea ice cover[15].

The development of a PDO-like response during the mid-Holocene also explains spatial patterns evident in our synthesis of North American hydroclimate changes. Collectively, rainfall-sensitive proxies show a pattern of widespread drying over the Southwest, wetter conditions over the Pacific Northwest, and drying over western Alaska during the mid-Holocene. This reconstructed "tripole" pattern of precipitation changes is only evident in simulations in which hemispheric warming excites a Pacific Ocean temperature response resembling the negative phase of the PDO (Fig. 3). The tripole pattern of precipitation anomalies is also characteristic of a negative phase of the PDO in instrumental data[35] (Extended Data Fig. 8). Simulations that are in higher agreement with proxy-inferred SST patterns also show increased agreement with

patterns of hydroclimate change as identified using the Cohen's kappa metric ($r = 0.358$, $p<0.001$; Fig. 3e). The correlation between the two metrics of agreement supports the role of the emergent PDO-like pattern in mediating the hydroclimatic response over the western US as a consequence of vegetation-driven hemispheric warming.

While it has been previously argued that the historical PDO is unforced because it can arise stochastically in climate model simulations, our results suggest that strong hemispheric warming, as occurred during the mid-Holocene, may induce a similar pattern, exacerbating Southwest drought. This raises the possibility that a similar response may occur due to ongoing and future greenhouse warming. To evaluate this, we analyzed changes in North Pacific climate over the recent 1982-2019 period of drought using a large (100-member) ensemble of coupled climate model simulations[36] driven by historical forcings. Ensembles of this size provide a mechanism for robustly isolating regional responses to external forcings in models[35]. The simulations show the emergence of a forced PDO-like pattern similar to observations (Fig. 4a,b). A similar pattern of warming is also evident in future simulations under enhanced greenhouse gas warming (SSP370) (Fig. 4c), suggesting that warming is driving a negative PDO-like state into the near future, which should lead to continued reduction in wintertime precipitation over the Southwest US.

Although the large ensemble of historical simulations produces a PDO-like pattern and induces drying over the Southwest US, the magnitude of precipitation decline is underestimated by ~68% when compared with observations[36,37] (Fig. 4a,b). Atmospheric simulations from the Global Ocean Global Atmosphere (GOGA) experiment, forced by historically prescribed SST patterns, including a negative PDO pattern, improve agreement with the instrumental precipitation data yet still significantly underestimate (~50%) winter precipitation deficits over the western US. However, in these experiments, most of the drying is driven by the observed shift towards a La Nina-like state in the tropical Pacific rather than the changes in North Pacific SSTs (Extended Data Fig. 7). The muted precipitation response in the GOGA experiments could indicate that the observed drought is stochastically generated via atmospheric dynamics, or conversely that simulated precipitation changes are insensitive to the development of a PDO-like pattern in the Pacific. However, a similar proxy-model discrepancy in the magnitude of winter precipitation decline is evident in our Holocene model-data comparison (Fig. 2, Extended Data Table 1). Together, these results suggest that models systematically underestimate the magnitude of the atmospheric response to hemispheric warming, even when a forced PDO emerges in response to these changes. Furthermore, simulations of future warming in response to anthropogenic greenhouse gases may similarly underestimate the impact on winter precipitation over the Southwest.

This study demonstrates that the early to mid-Holocene was characterized by a drought of exceptional severity and persistence, with winter precipitation deficits of at least 20% and potentially as much as 50% over the southern Rocky Mountains (Fig. 2b,d). Our hydroclimate proxy synthesis shows that this drying was part of a large-scale pattern of coupled ocean-atmosphere changes originating in the North Pacific. This climatic pattern resembles a modern negative phase of the PDO, but unlike this mode of variability, which is thought to be internally generated, it emerges as a forced response during the mid-Holocene. Models show that this response was activated by continental warming due to increased Northern Hemisphere

vegetation cover during this interval. Future simulations forced by anthropogenic greenhouse gases also show a negative PDO-like pattern, suggesting that the historical emergence of a PDO may be a forced response and that this pattern may persist into the future, influencing the hydroclimate of the western US. However, our results also suggest that the magnitude of wintertime precipitation reductions associated with this North Pacific SST response are underestimated in simulations of the mid-Holocene and the historical period. Models may severely underestimate the future risk of winter precipitation change in the Southwest US when the snowpack essential for maintaining large river systems such as the Colorado is produced. As a result, future drought is likely to be much more intense than indicated by current projections for water-dependent societies and ecosystems in North America.

Acknowledgements

We acknowledge the decades of work by many individual authors who produced the paleoclimate records used here in the sea surface temperature and hydroclimate data syntheses. We also wish to acknowledge the organizers and all the modelers who contributed mid-Holocene, simulations to the Paleoclimate Modeling Intercomparison Project, Phase 3 (PMIP3). The CESM project is supported primarily by the National Science Foundation (NSF). This material is based upon work supported by the National Center for Atmospheric Research (NCAR), which is a major facility sponsored by the NSF under Cooperative Agreement No. 1852977. The CAM6 Prescribed SST GOGA experiments were conducted by the Climate Variability and Climate Change Working Group (CVCWG).

Funding: This work was funded by US National Science Foundation P2C2 program awards 1702271 to T.M.S. and 2002528 to T.M.S. and P.D. F.S.R.P. acknowledges financial support from the NSERC Discovery Grant (grant RGPIN-2018-04981) and the NOVA - FRQNT-CRSNG (grants 2023-NOVA-324826; ALLRP 577112 - 22).

Author Contributions: Conceptualization: T.M.S., P.D., Methodology: T.M.S., P.D., V.T., Investigation: T.M.S., P.D., V.T., Sample collection: R.S.A., P.J.F., Climate simulations: F.P., A.L., J.T., Writing- original draft: V.T., T.M.S., P.D., Writing- review and editing: all authors.

Competing interests: Authors declare that they have no competing interests.

Data and materials availability: All data produced in our analyses are available in the main text or the supplementary materials. CESM2 simulations are available for download from http://www.cesm.ucar.edu/experiments/. PMIP3 model output is publicly available from https://pmip3.lsce.ipsl.fr. Model output from all additional simulations available upon request.

Figures

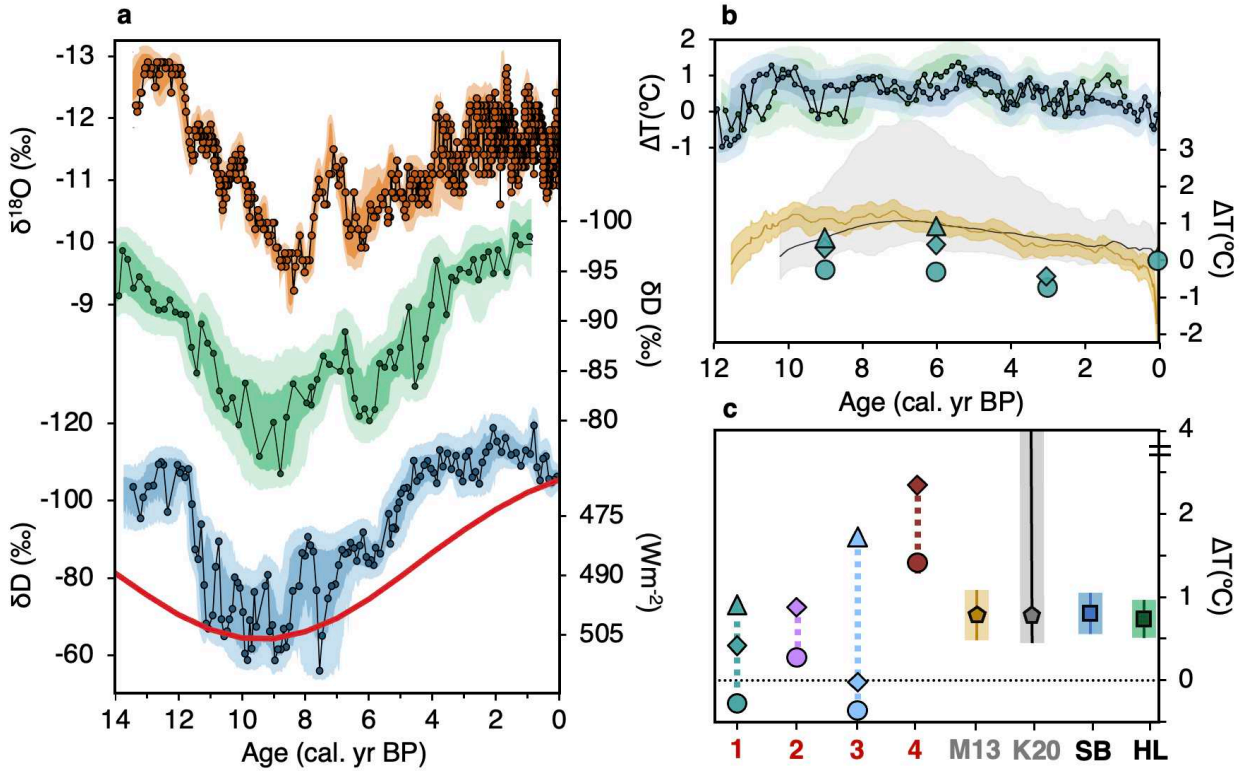

Fig.1. Proxy paleoclimate changes in the southwest US. a. High resolution stable isotope records reflecting moisture source changes over the past 14 ka from: Leviathan Cave (orange) in Nevada[12], Hunters Lake (HL) (green) in southern Colorado (this study), Stewart Bog (SB) (blue) in the Sangre de Cristo Mountains of northern New Mexico (this study). **b.** simulated temperature anomalies[15] and paleotemperature reconstructions over the past 12 ka: Hunters Lake MBT'$_{5ME}$ lake temperature (green), Stewart bog MBT'$_{5ME}$ soil temperature (blue), multiproxy temperature syntheses for 30-90°N[27-28]. Shading indicates 1σ and 2σ uncertainties in the reconstructions. **c.** 6 ka 30-90°N temperature anomalies in 1-CESM1.2, 2-CCSM4-Toronto, 3-GISS-E2-G, and 4-EC-Earth without vegetation change (circles), with prescribed "Green Sahara" (diamonds), and with both high and low latitude prescribed vegetation (triangles) compared with M13[27] and K20[28] paleotemperature reconstructions and our reconstructions (SB and HL).

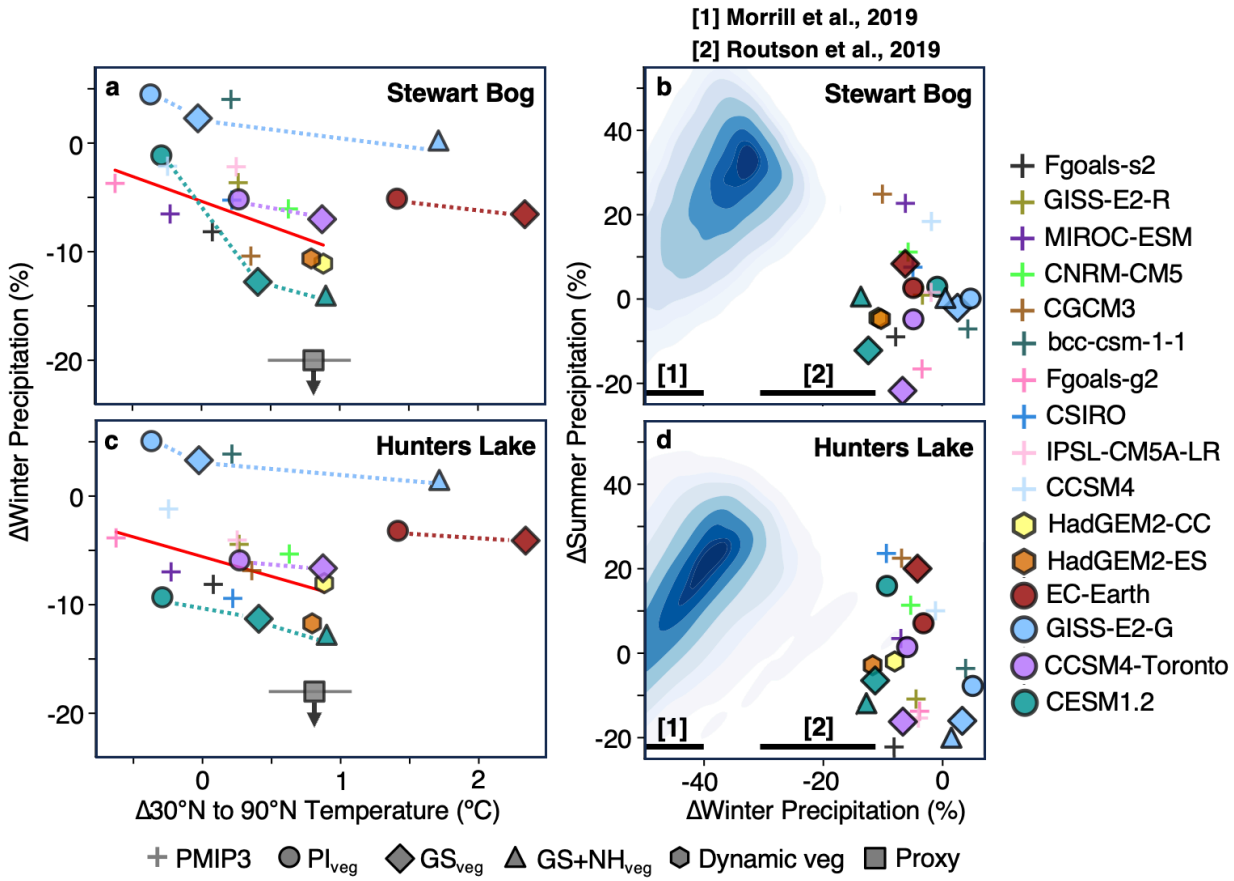

Fig. 2. Model and proxy estimates of mid-Holocene (6 ka) winter precipitation anomalies. **a-c.** Simulated Northern Hemisphere temperature (30-60°N) and winter precipitation anomalies at **a.** Stewart Bog and **c.** Hunters Lake illustrating the systematic decrease in winter precipitation with hemispheric warming in PMIP3 models (crosses), with interactive vegetation (hexagon) and in models without vegetation change (circles), with prescribed "Green Sahara" (diamonds), and with both high and low latitude prescribed vegetation (triangles). Comparison of model estimates of winter and summer precipitation during the mid-Holocene (symbols as in **a,c**) against Bayesian isotope mixing model estimates of mid Holocene leaf wax isotope values (blue shading). The range of estimates of mid-Holocene drying based on [1] pollen data[11] and [2] lake water balance modeling[32] are shown by black lines in **b**,**d** for comparison.

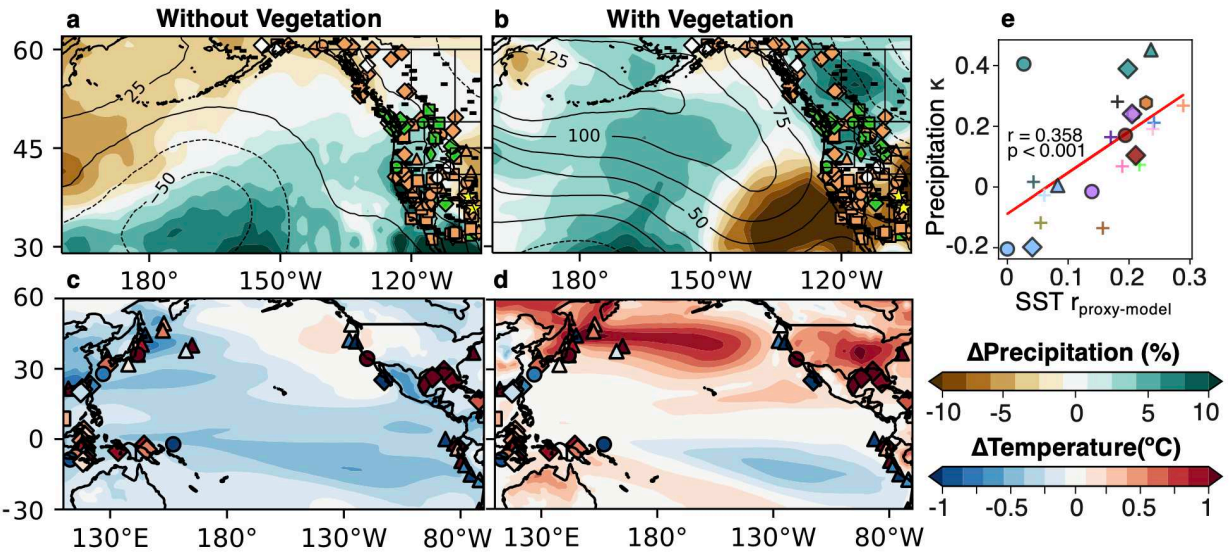

Fig. 3. Proxy model data comparison for the mid Holocene. a-b. Ensemble mean precipitation (shading) and sea level pressure anomalies and (**c,d**) surface temperature anomalies (shading) for models without (left) and with vegetation and hemispheric warming (right). Symbols (same as Fig.2) indicate proxy data sites used to assess agreement. **e.** The maximum precipitation Cohen's κ value vs. the sea surface temperature pattern correlation value for all the models.

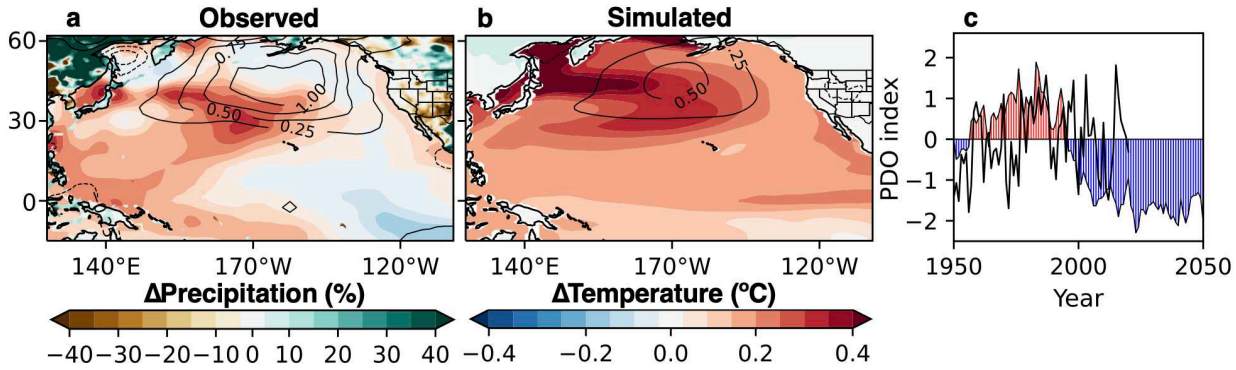

Fig. 4. Emergence of a PDO pattern and southwest drought in observations, models and the future. a-b. Maps of sea surface temperature (shading), winter precipitation (shading), and sea level pressure (contours) trends between 1982 and 2019 in: **a.** observations[37,38,39], **b.** a 100-member ensemble of fully coupled climate model simulations forced with historical greenhouse gas emissions[36]. **c.** Projected (shading) changes in the normalized winter (DJF) PDO index[41] from a 100-member ensemble of climate simulations forced by future predicted greenhouse gas emissions[36] compared with observations[39] (line).

References

1. A. P. Williams, B. I. Cook, J. E. Smerdon, Rapid intensification of the emerging southwestern North American megadrought in 2020-2021. *Nature Climate Change* **12**, 232-+ (2022).
2. F. Lehner, C. Deser, I. R. Simpson, L. Terray, Attributing the US Southwest's Recent Shift Into Drier Conditions. *Geophysical Research Letters* **45**, 6251-6261 (2018).
3. G. J. McCabe, M. A. Palecki, J. L. Betancourt, Pacific and Atlantic Ocean influences on multidecadal drought frequency in the United States. *Proceedings of the National Academy of Sciences of the United States of America* **101**, 4136-4141 (2004).
4. S. Schubert, D. Gutzler, H. Wang, A. Dai, T. Delworth, C. Deser, K. Findell, R. Fu, W. Higgins, M. Hoerling, B. Kirtman, R. Koster, A. Kumar, D. Legler, D. Lettenmaier, B. Lyon, V. Magana, K. Mo, S. Nigam, P. Pegion, A. Phillips, R. Pulwarty, D. Rind, A. Ruiz-Barradas, J. Schemm, R. Seager, R. Stewart, M. Suarez, J. Syktus, M. Ting, C. Wang, S. Weaver, N. Zeng, A US CLIVAR Project to Assess and Compare the Responses of Global Climate Models to Drought-Related SST Forcing Patterns: Overview and Results. *Journal of Climate* **22**, 5251-5272 (2009).
5. P. Chylek, M. K. Dubey, G. Lesins, J. N. Li, N. Hengartner, Imprint of the Atlantic multi-decadal oscillation and Pacific decadal oscillation on southwestern US climate: past, present, and future. *Climate Dynamics* **43**, 119-129 (2014).
6. C. Zhao, B. Liu, S. Piao, X. Wang, D. B. Lobell, Y. Huang, M. Huang, Y. Yao, S. Bassu, P. Ciais, J. Durand, J. Elliott, F. Ewert, I. A. Janssens, T. Li, E. Lin, Q. Liu, P. Martre, C. Müller, S. Peng, J. Peñuelas, A. C. Ruane, D. Wallach, T. Wang, D. Wu, Z. Liu, Y. Zhu, Z. Zhu, S. Asseng, Temperature increase reduces global yields of major crops in four independent estimates. *Proceedings of the National Academy of Sciences of the United States of America* **114**, 9326-9331 (2017).
7. M. P. Erb, J. Emile-Geay, G. J. Hakim, N. Steiger, E. J. Steig, Atmospheric dynamics drive most interannual US droughts over the last millennium. *Science Advances* **6**, (2020).
8. J. Scheff, D.M.W. Frierson, Scaling potential evapotranspiration with greenhouse warming. Journal of Climate **27**, 1539–1558 (2004).
9. N. S. Diffenbaugh, D. L. Swain, D. Touma, Anthropogenic warming has increased drought risk in California. *Proceedings of the National Academy of Sciences of the United States of America* **112**, 3931-3936 (2015).
10. N. W. Hermann, J. L. Oster, D. E. Ibarra, Spatial patterns and driving mechanisms of mid-Holocene hydroclimate in western North America. *Journal of Quaternary Science* **33**, 421-434 (2018).
11. C. C. Routson, N. P. McKay, D. S. Kaufman, M. P. Erb, H. Goosse, B. N. Shuman, J. R. Rodysill, T. Ault, Mid-latitude net precipitation decreased with Arctic warming during the Holocene. *Nature* **568**, 83-+ (2019).
12. M. S. Lachniet, Y. Asmerom, V. Polyak, R. Denniston, Great Basin Paleoclimate and Aridity Linked to Arctic Warming and Tropical Pacific Sea Surface Temperatures. *Paleoceanography and Paleoclimatology* **35**, (2020).
13. S. E. Metcalfe, J. A. Barron, S. J. Davies, The Holocene history of the North American Monsoon: 'known knowns' and 'known unknowns' in understanding its spatial and temporal complexity. *Quaternary Science Reviews* **120**, 1-27 (2015).

14. H. S. Park, S. J. Kim, A. L. Stewart, S. W. Son, K. H. Seo, Mid-Holocene Northern Hemisphere warming driven by Arctic amplification. *Science Advances* **5**, (2019).
15. A. J. Thompson, J. Zhu, C. J. Poulsen, J. E. Tierney, C. B. Skinner, Northern Hemisphere vegetation change drives a Holocene thermal maximum. *Science Advances* **8**, (2022).
16. C. C. Routson, M. P. Erb, N. P. McKay, High Latitude Modulation of the Holocene North American Monsoon. *Geophysical Research Letters* **49**, (2022).
17. T. Bhattacharya, An Energetic Perspective on the Holocene North American Monsoon. *Geophysical Research Letters* **49**, (2022).
18. B. J. Hoskins, K. I. Hodges, The Annual Cycle of Northern Hemisphere Storm Tracks. Part I: Seasons. *Journal of Climate* **32**, 1743-1760 (2019).
19. G. Jimenez-Moreno, P. J. Fawcett, R. S. Anderson, Millennial- and centennial-scale vegetation and climate changes during the late Pleistocene and Holocene from northern New Mexico (USA). *Quaternary Science Reviews* **27**, 1442-1452 (2008).
20. P. Martinez-Sosa, J. E. Tierney, I. C. Stefanescu, E. D. Crampton-Flood, B. N. Shuman, C. Routson, A global Bayesian temperature calibration for lacustrine brGDGTs. *Geochimica Et Cosmochimica Acta* **305**, 87-105 (2021).
21. E. D. Crampton-Flood, J. E. Tierney, F. Peterse, F. Kirkels, J. S. S. Damste, BayMBT: A Bayesian calibration model for branched glycerol dialkyl glycerol tetraethers in soils and peats. *Geochimica Et Cosmochimica Acta* **268**, 142-159 (2020).
22. D. Sachse , I. Billault, G. J. Bowen, Y. Chikaraishi, T. E. Dawson, S. J. Feakins, K. H. Freeman, C. R. Magill, F. A. McInerney, M. T. J. van der Meer, P. Polissar, R. J. Robins, J. P. Sachs, H. Schmidt, A. L. Sessions, James W.C. White, Jason B. West, Ansgar Kahmen, Molecular Paleohydrology: Interpreting the Hydrogen- Isotopic Composition of Lipid Biomarkers from Photosynthesizing Organisms. *Annual Review of Earth and Planetary Sciences, Vol 40* **40**, 221-249 (2012).
23. D. G. Tolley, M. D. Frisbee, A. R. Campbell. (New Mexico Geological Society, Guidebook, 2015), vol. 66th Field Conference, chap. Geology of the Las Vegas Region, pp. 303-312.
24. G. J. Bowen, J. Revenaugh, Interpolating the isotopic composition of modern meteoric precipitation. *Water Resources Research* **39**, (2003).
25. C. L. Tulley-Cordova, A. L. Putman, G. J. Bowen, Stable Isotopes in Precipitation and Meteoric Water: Sourcing and Tracing the North American Monsoon in Arizona, New Mexico, and Utah. *Water Resources Research* **57**, (2021).
26. P. Braconnot, M. Kageyama, Shortwave forcing and feedbacks in Last Glacial Maximum and Mid-Holocene PMIP3 simulations. *Philosophical Transactions of the Royal Society a-Mathematical Physical and Engineering Sciences* **373**, (2015).
27. S. A. Marcott, J. D. Shakun, P. U. Clark, A. C. Mix, A Reconstruction of Regional and Global Temperature for the Past 11,300 Years. *Science* **339**, 1198-1201 (2013).
28. D. Kaufman, N. McKay, C. Routson, M. Erb, C. Dätwyler, P. S. Sommer, O. Heiri, B. Davis, Holocene global mean surface temperature, a multi-method reconstruction approach. *Scientific Data* **7**, (2020).
29. J. R. Stone, S. C. Fritz, Multidecadal drought and Holocene climate instability in the Rocky Mountains. *Geology* **34**, 409-412 (2006).
30. B. Shuman, A. K. Henderson, S. M. Colman, J. R. Stone, S. C. Fritz, L. R. Stevens, M. J. Power, C. Whitlock, Holocene lake-level trends in the Rocky Mountains, USA. *Quaternary Science Reviews* **28**, 1861-1879 (2009).

31. B. N. Shuman, P. Pribyl, J. Buettner, Hydrologic changes in Colorado during the mid-Holocene and Younger Dryas. *Quaternary Research* **84**, 187-199 (2015).
32. C. Morrill, E. Meador, B. Livneh, D. T. Liefert, B. N. Shuman, Quantitative model-data comparison of mid-Holocene lake-level change in the central Rocky Mountains. *Climate Dynamics* **53**, 1077-1094 (2019).
33. C. C. Routson, D. S. Kaufman, N. P. McKay, N. P. Erb, S. H. Arcusa, K. J. Brown, K. J., Kirby, J. P. Marsicek, R. S. Anderson, G. Jiménez-Moreno, J. R. Rodysill, M. S. Lachniet, S. C. Fritz, J. R. Bennett, M. F. Goman, S. E. Metcalfe, J. M. Galloway, G. Schoups, D. B. Wahl, J. L. Morris, F. Staines-Urías, A. Dawson, B. N. Shuman, D. G. Gavin, J. S. Munroe, B. F. Cumming, A multiproxy database of western North American Holocene paleoclimate records. *Earth System Science Data* **13**, 1613-1632 (2021).
34. M. Newman, M. A. Alexander, T. R. Ault, K. M. Cobb, C. Deser, E. D. Lorenzo, N. J. Mantua, A. J. Miller, S. Minobe, H. Nakamura, N. Schneider, D. J. Vimont, A. S. Phillips, J. D. Scott, C. A. Smith, The Pacific Decadal Oscillation, Revisited, *Journal of Climate* **29**, 4399-4427 (2016).
35. C. Deser, A. S. Phillips, J. W. Hurrell, Pacific interdecadal climate variability: Linkages between the tropics and the North Pacific during boreal winter since 1900. *Journal of Climate* **17**, 3109-3124 (2004).
36. K. B. Rodgers, S. Lee, N. Rosenbloom, A. Timmermann, G. Danabasoglu, C. Deser, J. Edwards, J. Kim, I. R. Simpson, K. Stein, M. F. Stuecker, R. Yamaguchi, T. Bódai, E. Chung, L. Huang, W. M. Kim, J. Lamarque, D. L. Lombardozzi, W. R. Wieder, S. G. Yeager, Ubiquity of human-induced changes in climate variability. *Earth System Dynamics* **12**, 1393-1411 (2021).
37. U. Schneider, A. Becker, P. Finger, E. Rustemeier, M. Ziese, GPCC Full Data Monthly Product Version 2020 at 1.0°: Monthly Land-Surface Precipitation from Rain-Gauges built on GTS-based and Historical Data, (2020).
38. E. Kalnay, M. Kanamitsu, R. Kistler, W. Collins, D. Deaven, L. Gandin, M. Iredell, S. Saha, G. White, J. Woollen, Y. Zhu, M. Chelliah, W. Ebisuzaki, W. Higgins, J. Janowiak, K. C. Mo, C. Ropelewski, J. Wang, A. Leetmaa, R. Reynolds, R. Jenne, D. Joseph, The NCEP/NCAR 40-year reanalysis project, *Bull. Amer. Meteor. Soc.* **77**, 437-470 (1996).
39. B. Huang, P.W. Thorne, V.F. Banzon, T. Boyer, G. Chepurin, J.H. Lawrimore, M.J. Menne, T.M. Smith, R.S. Vose, H.Zhang, NOAA Extended Reconstructed Sea Surface Temperature (ERSST) **5**. NOAA National Centers for Environmental Information (2017).
40. Phillips, A. S., C. Deser, J Fasullo, D. P. Schneider and I. R. Simpson, Assessing Climate Variability and Change in Model Large Ensembles: A User's Guide to the Climate Variability Diagnostics Package for Large Ensembles (2020).

Methods

Study sites and age modeling

Stewart Bog is located in the Sangre de Cristo mountains of Northern New Mexico (latitude: 35.83, longitude: -105.73, elevation: 3119 meters) (Extended Data Fig.1). It was formed in a depression in the landscape created by glacial retreat ca. 14.7 ka[41]. The composite Stewart Bog record is based on three sediment cores: B1-4, B1-5, and B1-6, obtained using a Livingston square-rod piston corer[41]. The age model for this composite core is based on the radiocarbon dating[41] of bulk organic carbon (n=5), charcoal (n=2), and wood (n=4). In this study, we updated the sediment age-depth model using the IntCal20 calibration curve and the Bayesian age modeling program RBACON[42].

Hunters Lake is a subalpine lake in the Southern Rockies (latitude: 37.36, longitude: -106.50, elevation: 3516 meters). A long sediment core was retrieved using a modified Livingston piston corer, and a short core capturing the surface sediments was obtained to provide an uninterrupted lake record extending to the present[43]. Six radiocarbon dates were obtained from the long sediment core, and ^{137}C and ^{210}Pb dating techniques were used to generate an age model for the uppermost surface core to establish an age model[43]. The sediment age-depth model was updated for this study using the IntCal20 calibration curve and the Bayesian age modeling program RBACON[42].

Sampling and sample preparation

One cc samples were taken every 4 cm from the Stewart Bog and Hunters Lake cores. At Hunters Lake, we were unable to sample the uppermost short core because insufficient material remained for analysis. Lipids were extracted from freeze-dried sediments using MARS 5 Xpress microwave solvent extraction system using dichloromethane (DCM): methanol (MeOH) (9:1, v:v). Lipid extraction was performed by ramping the temperature slowly to 100ºC and holding for 10 minutes with continuous stirring. After extraction, samples were filtered and dried over a NaSO4 column and evaporated under N_2. Total lipid fractions were loaded onto aminopropyl columns for solid phase extraction using Rapid Trace SPE stations and separated with hexane, isopropanol in hexane, and 2% formic acid in DCM to isolate the apolar, GDGT, and fatty acid fractions, respectively. The fatty acid fractions were then methylated in an acidified methanol solution (12 hours at 50°C). The resultant fatty acid methyl esters (FAMEs) were purified again over silica gel using dichloromethane prior to quantification and analysis.

GDGT analysis

The GDGT fraction was analyzed via high-performance liquid chromatography–atmospheric pressure chemical ionization mass spectrometry (HPLC-APCI-MS) on an Agilent 1200 HPLC instrument fitted with two UHPLC silica columns (BEH HILIC columns, 2.1 × 150 mm, 1.7 μm; Waters), and a 2.1 × 5 mm pre-column of the same material (Waters). Separation of the GDGTs was performed at a flow rate of 0.2 ml/min using the following schedule: isocratic elution for 25 min with 18% B, a gradient to 35% B in 25 min, a gradient to 100% B in 30 min (A: n-hexane; B: n-hexane: isopropanol (9/1)). The column was backflushed with 100% B for 10 minutes and re-equilibrated for 20 min after each sample. The mass spectrometer was operated in single ion monitoring (SIM) mode using m/z 1022, 1020, 1018, 1036, 1034, 1032, 1050, 1048, 1046 for the branched GDGTs Ia, Ib, Ic, IIa, IIb, IIc, IIIa, IIIb, IIIc, respectively. The relative abundance of individual brGDGTs was determined by integrating the peak areas of the protonated molecule using Agilent Chemstation software.

Stable isotope analysis of FAMEs

Prior to stable isotope analysis, the fatty acid fraction of all samples was analyzed (as FAMES) by gas chromatography flame ionization detection to assess purity and determine the concentrations of the target compounds. Hydrogen isotope analysis was performed by gas chromatography-pyrolysis-isotope ratio mass spectrometry on a Thermo Finnigan Delta V Plus mass spectrometer. Hydrogen reference gas and an internal propane gas standard were calibrated against a known n-alkane standard (the "B4" mix, A. Schimmelmann, Indiana University). An external FAME standard was analyzed multiple times during each run, and multiple injections of the propane gas standard were run with each sample and used to correct for sample drift and offsets. Samples were run in duplicate or triplicate, and standard deviations between injections were ~2‰ versus VSMOW. A mass balance correction was applied to account for the added methyl group during methylation. The δD values of the methylation methanol were determined by methylating a phthalic acid standard of known isotopic composition. In this study, we focus on the isotopic composition of the long-chain fatty acids (C_{28}, C_{30}) because they are less likely to be produced by aquatic or microbial sources.

MBT'5ME Paleotemperature Reconstructions

We used the MBT'5ME index (Methylation of 5 Methyl Branched Tetraethers) to compute temperatures for Hunters Lake and Stewart Bog from GDGT abundances. The MBT'5ME index is calculated following[44].

$$MBT'_{5ME} = \frac{Ia + Ib + Ic}{Ia + Ib + Ic + IIa + IIb + IIc + IIIa + IIIb + IIIc}$$

Several empirical calibrations have been developed for the MBT'5ME – temperature relationship using modern lake surface sediments[20] and soils[21]. In this study, we employ the Bayesian calibration approaches implemented by[20,21]. For Hunters Lake, which appears to have been a lake system for its entire history, we use the lake calibration dataset from ref.[20]. At the Stewart Bog site, we assumed the branched dialkyl glycerol tetraether (brGDGT) signal was primarily sourced from soil-derived lipids. The similarity between the computed MBT'5ME temperature (2.8°C) of the surface sediments and the current mean annual air temperature at the site (~3°C) is consistent with this assertion.

Inferring δD_{precip} from δD_{wax}

Previous syntheses of modern leaf wax samples have shown that leaf wax δD can provide a reliable archive of the past isotopic composition of precipitation source water[43]. However, a few complicating factors relating δD_{wax} to δD_{precip} need to be considered when interpreting leaf wax reconstructions. First, there is a strong biological fractionation associated with the process of leaf wax synthesis (ε_{wax}), which has been shown to vary as a function of plant type and biosynthetic pathway[22]. In proxy records, sedimentary δD_{wax} values reflect the combined biosynthetic fractionation of all the plants in the catchment, potentially complicating the interpretation of leaf wax records. To quantitatively estimate the impact of these changes in our records, we estimated the relative abundance of C_3 and C_4 plants in this record using existing pollen data[19,43]. Between 6ka and PI, there may have been as large as a 10% change in the abundance of C_3 plants (arboreal trees)[19,43]. Previous studies have suggested that there may be as

much as a 19‰ offset in the fractionation factors for plants with these two photosynthetic pathways ($\varepsilon_{wax\text{-}C3}$ =-113‰; $\varepsilon_{wax\text{-}C4}$ = -132‰)[23,45]. Given the changes in community plant composition indicated by the pollen data, this would have resulted in a shift in the fractionation factor of ~3‰ at Stewart Bog between the preindustrial and mid-Holocene[23,45]. This difference is within the errors of the mixing model calculations and likely the uncertainties in the estimates of endmember fractionation factors, so we did not apply any correction to the δD_{wax} data in this study. Evaporative fractionation can also cause offsets between the δD_{wax} and δD_{precip} values due to isotopic enrichment of the source water at the locus of leaf wax synthesis. While this effect can be large in arid regions, studies of modern plants across the Southwestern US indicate that the offset between δD_{wax} and δD_{precip} is indistinguishable within uncertainties throughout the hydrologic year[45]. Given the uncertainties associated with any correction for plant water evaporation, we did not make any adjustments for this effect in our analysis.

Bayesian Isotope Mixing Model

A Bayesian stable isotope mixing model was developed to estimate the proportion of seasonal moisture sources contributing to the stable isotope composition of a sample. For the publicly available MixSIAR Bayesian stable mixing model[46] used in this study, the following basic equation applies:

$$Y_j = \sum_k p_k \mu_{jk}^s$$

Where for each of the *j* tracers, the mixture tracer value, Y_j is equal to the sum of the *k* source tracer means μ_{jk}^s multiplied by their proportional contribution to the mixture (p_k). Mixing models assume that 1) the sources contributing to the mixture are known and quantified, 2) tracers are conserved through the mixing process, 3) source mixture and tracer values are fixed (known and invariant), 4) the p_k terms sum to unity, and 5) source tracer values differ[45]. The isotopic compositions of the modern precipitation sources for the Stewart Bog[23] and the Hunters Lake[24] sites were obtained to implement the model (Extended Data Fig.1).

In this study, a major assumption is that the dominant control on past changes in the isotopic composition of precipitation between the mid-Holocene and the pre-industrial is changes in the proportions of winter and summer precipitation. This assumption is based on previous studies, which indicated significant changes in the strength of the mid-Holocene monsoon and the winter storm track[10,12,16]. For this reason, these paleo isotopic values are represented as a two-end member mix between the monsoon and winter precipitation. The "raw" lists of stable isotope measurements from the winter and summer seasons were used as priors in the model to preserve the uncertainty in the estimates for the source means and variances. These winter and summer isotopic values were represented as uniform prior distributions:

$$p_1 \sim U(0,1) = \; p_1 \sim U(0,1)$$
$$\sum_{i=1}^{n=2} p_i = 1$$
$$p_2 = 1 - p_1$$

MixSIAR assumes multivariate normality and estimates the variance-covariance matrix associated with the tracers for each source. Naïve priors were used for winter and summer

precipitation proportions to reduce bias. The model was evaluated for two different times: the mid-Holocene and the pre-industrial. The "raw" lists of stable isotope measurements from the mid-Holocene (6±0.2 ka) and the pre-industrial (1850 to 1950 cal yr) were used to construct normal distributions for the isotopic values of the mixtures. Process and residual error with covariance were incorporated into the model. Posterior distributions of the proportion of summer to winter precipitation during the mid-Holocene and pre-industrial were used to calculate the percent change in winter and summer precipitation.

Seasonal pre-industrial precipitation amount data was retrieved from the ERA5 reanalysis data set[47]. Firstly, the distribution of the proportions of summer to winter precipitation during the pre-industrial calculated from the proxy records and the distribution of pre-industrial seasonal precipitation amounts (ERA5 reanalysis) were compared via bootstrapping to calculate the possible combinations of winter and summer precipitation that would satisfy the proxy calculated ratios. Next, we made the assumption that the sum of winter and summer precipitation during the mid-Holocene was less than that during the pre-industrial. Then, 10000 times we solved the equation:

$MH_{winter} + MH_{summer} \leq PI_{total}$

Where $MH_{summer} = MH_{ratio} \times MH_{winter}$

MH_{total} is a half-normal distribution centered around the PI_{total} with the same standard deviation as the PI_{total}; the assumption of this parametric shape was derived from the climate models, which show a shift in the mean precipitation during the mid-Holocene with the same standard deviation as during the pre-industrial. For each realization of pre-industrial and mid-Holocene seasonal precipitation amounts, the percent change in precipitation was calculated, leading to the simulated range in possible values.

Synthesis of Proxy Precipitation and SST Records

Proxy records were selected from the published literature that spanned at least the last 6 ka and could constrain the changes between the mid-Holocene and the pre-Industrial. Hydroclimate records were compiled from both existing syntheses[10,12,34], and were supplemented by new records from critical sites in the Pacific Northwest, Alaska, and the central US. For the pollen-inferred hydroclimate changes, we deviated from the interpretations used in previous syntheses and relied on the LegacyClimate 1.0 database of modern analog technique (MAT)- based pollen transfer functions[48]. Only those sites showing a statistically significant precipitation reconstruction were included. For Pacific sea surface temperatures, we used the compilation of Osman et al.,[49] and supplemented it with additional sites from the published literature.

We used mean values for the mid-Holocene (6000±500 yr BP) and Pre-industrial (200 to 500 yr BP) to compute anomalies. To classify the hydroclimatic and sea surface temperature data from each site, a T-test was used first to determine if the changes were statistically significant, given the variability in the reconstructions. All sites were then classified as wetter, drier, warmer, cooler, or unchanged relative to the preindustrial.

Climate model experiments

To understand how the climate system changes under mid-Holocene conditions in climate model simulations, we compiled 24 existing mid-Holocene (6 ka) simulations performed with 17 general circulation models (GCMs). Of these, 13 simulations were from the Paleoclimate Modelling Intercomparison Project phase III (PMIP3) project, including two which

included dynamic vegetation changes (HadGEM2-CC, HadGEM2-ES). We also included 11 additional simulations, which allowed us to assess the influence of changes in prescribed vegetation. In two cases (CESM1.2 and GISS-E2), models were run with preindustrial vegetation, prescribed vegetation over the Sahara (e.g., "Green Sahara" runs), and prescribed vegetation over the Northern Hemisphere + "Green Sahara". Mid-Holocene simulations were forced by prescribing greenhouse gas concentrations and astronomical parameters to their values at 6 ka. Anomalies were calculated for each simulation by subtracting values from pre-Industrial and mid-Holocene simulations. Note that in each of the simulations, vegetation over North Africa was prescribed differently. In CESM1.2 simulation, modern-day Sahelian land surface and vegetation at 11°N were prescribed everywhere north of the latitude. In EC-Earth 3.1, Sahara vegetation was prescribed as shrub. In the UofT-CCSM4 simulation the Sahara was covered by evergreen shrubs up to 25°N and replaced by a steppe/savanna mix over the rest of North Africa. In GISS-E2.1-G, grass and soil cover was replaced by shrub below 25°N and by grassland over the rest of North Africa. In the simulations with expanded northern hemisphere vegetation, areas with modern day C_3 grass cover were replaced with deciduous forest.

Proxy-model comparison

To evaluate which climate models most accurately reflect the patterns of SST and hydroclimate changes evident in the proxy data, we followed the approach devised previously in DiNezio and Tierney,[50] and computed the weighted Cohen's kappa statistic. This approach categorizes the proxy and model data at each location (wet, dry, unchanged or warmer, cooler, unchanged, relative to the preindustrial) and varies the threshold used to determine this categorization to evaluate the robustness of the results (Extended Data Fig.5). The agreement is estimated using the weighted Cohen's k statistic, which is the fractional agreement between the proxy and model data at all sites compared to the probability of random agreement. The weighting procedure penalizes sites more when the Holocene-PI change is in the opposite direction between the models and the proxy reconstructions. Because the proxy data is not distributed evenly in space, and to avoid overrepresenting some areas in the model where proxy data density is higher, we applied a 100 km search radius to each site and combined all proxy data reconstructions within that area following DiNezio and Tierney[50].

References

41. J. Armour, P. J. Fawcett, J. W. Geissman, 15 k.y. paleoclimatic and glacial record from northern New Mexico. *Geology* **30**, 723-726 (2002).
42. M. Blaauw, J. A. Christen, Flexible Paleoclimate Age-Depth Models Using an Autoregressive Gamma Process. *Bayesian Analysis* **6**, 457-474 (2011).
43. R. S. Anderson, C. D. Allen, J. L. Toney, R. B. Jass, A. N. Bair, Holocene vegetation and fire regimes in subalpine and mixed conifer forests, southern Rocky Mountains, USA. *International Journal of Wildland Fire* **17**, 96-114 (2008).
44. C. De Jonge, E. C. Hopmans, A. Stadnitskaia, W. I. C. Rijpstra, R. Hofland, E. Tegelaar, J. S. S. Damsté, Identification of novel penta- and hexamethylated branched glycerol dialkyl glycerol tetraethers in peat using HPLC-MS2, GC-MS and GC-SMB-MS. *Organic Geochemistry* **54**, 78-82 (2013).
45. J. Z. Hou, W. J. D'Andrea, Y. S. Huang, Can sedimentary leaf waxes record D/H ratios of continental precipitation? Field, model, and experimental assessments. *Geochimica Et Cosmochimica Acta* **72**, 3503-3517 (2008).
46. B. C. Stock, A. L. Jackson, E. J. Ward, A. C. Parnell, D. L. Phillips, B. X. Semmens, Analyzing mixing systems using a new generation of Bayesian tracer mixing models. *Peerj* **6**, (2018).
47. H. Hersbach, B. Bell, P. Berrisford, S. Hirahara, A. Horányi, J. Muñoz-Sabater, J. Nicolas, C. Peubey, R. Radu, D. Schepers, A. Simmons, C. Soci, S. Abdalla, X. Abellan, G. Balsamo, P. Bechtold, G. Biavati, J. Bidlot, M. Bonavita, N. Thépaut, The ERA5 global reanalysis. *Quarterly Journal of the Royal Meteorological Society* **146**, 1999-2049 (2020).
48. U. Herzschuh, T. Böhmer, C. Li, M. Chevalier, R. Hébert, A. Dallmeyer, X. Cao, N. H. Bigelow, L. Nazarova, E. Y. Novenko, J. Park, O. Peyron, N. A. Rudaya, F. Schlütz, L. S. Shumilovskikh, P. E. Tarasov, Y. Wang, R. Wen, Q. Xu, Z. Zheng, LegacyClimate 1.0: a dataset of pollen-based climate reconstructions from 2594 Northern Hemisphere sites covering the last 30 kyr and beyond, *Earth Syst. Sci. Data*, **15**, 2235–2258, https://doi.org/10.5194/essd-15-2235-2023, 2023.
49. M. B. Osman, J. E. Tierney, J. Zhu, R. Tardif, G. J. Hakim, J. King, C. J. Poulsen, Globally resolved surface temperatures since the Last Glacial Maximum. *Nature* **599**, 239-244 (2021).
50. P. N. DiNezio, J. E. Tierney, The effect of sea level on glacial Indo-Pacific climate. *Nature Geoscience* **6**, 485-491 (2013).
51. H. M. Zhang, B. Huang, J. Lawrimore, M. Menne, T. M. Smith, NOAA Global Surface Temperature Dataset (NOAAGlobalTemp), Version 5.0. NOAA National Centers for Environmental Information (2019).
52. P. D. Jones, D. H. Lister, T. J. Osborn, C. Harpham, M. Salmon, C. P. Morice, Hemispheric and large-scale land surface air temperature variations: an extensive revision and an update to 2010. *Journal of Geophysical Research*, (2012).

Extended Data

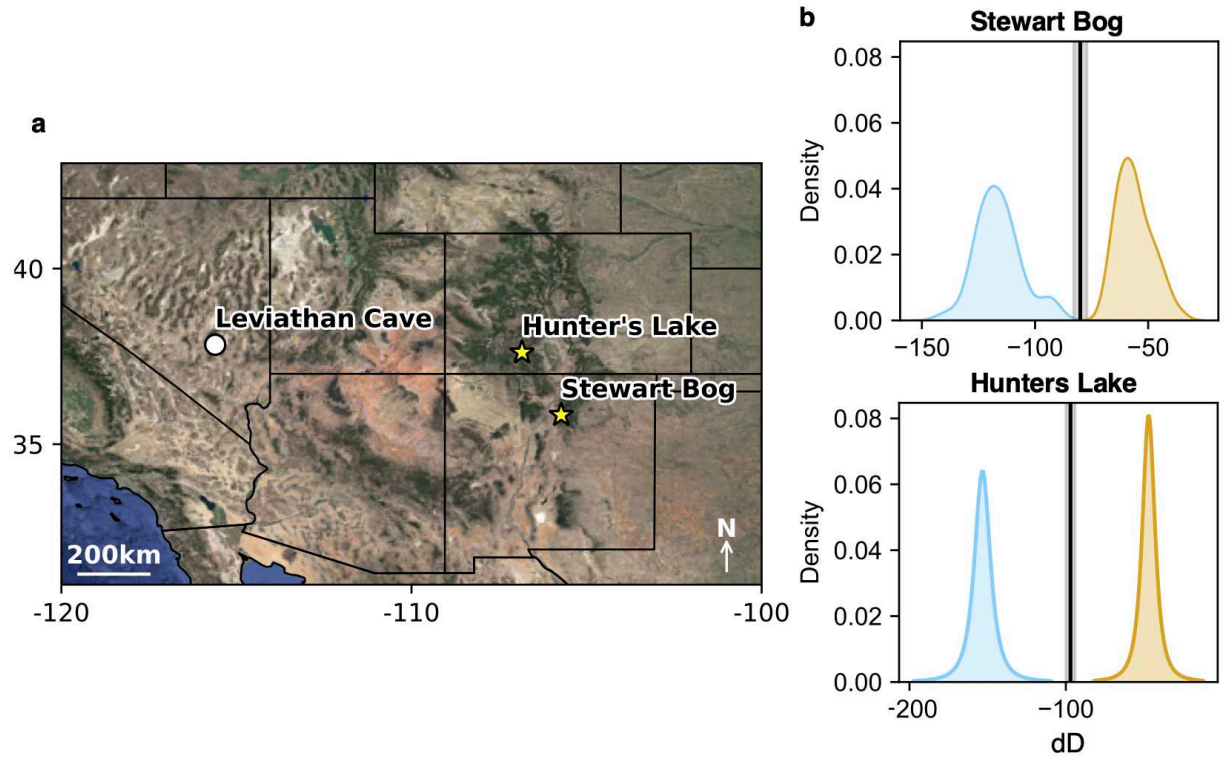

Extended Data Fig. 1.

a. Map of the Southwest US shown with the locations of the sites in this study, Stewart Bog and Hunters Lake, as well as the Leviathan Cave site. Satellite imagery from Stamen Design, under CC BY 3.0. Data by OpenStreetMap, under ODbL. **b.** Probability density plots of modern δD seasonal precipitation data from Stewart Bog, NM[23] and Hunters Lake, CO[24] and average annual precipitation stable isotopic values from OIPC[24] (black line) with 95% CI in gray.

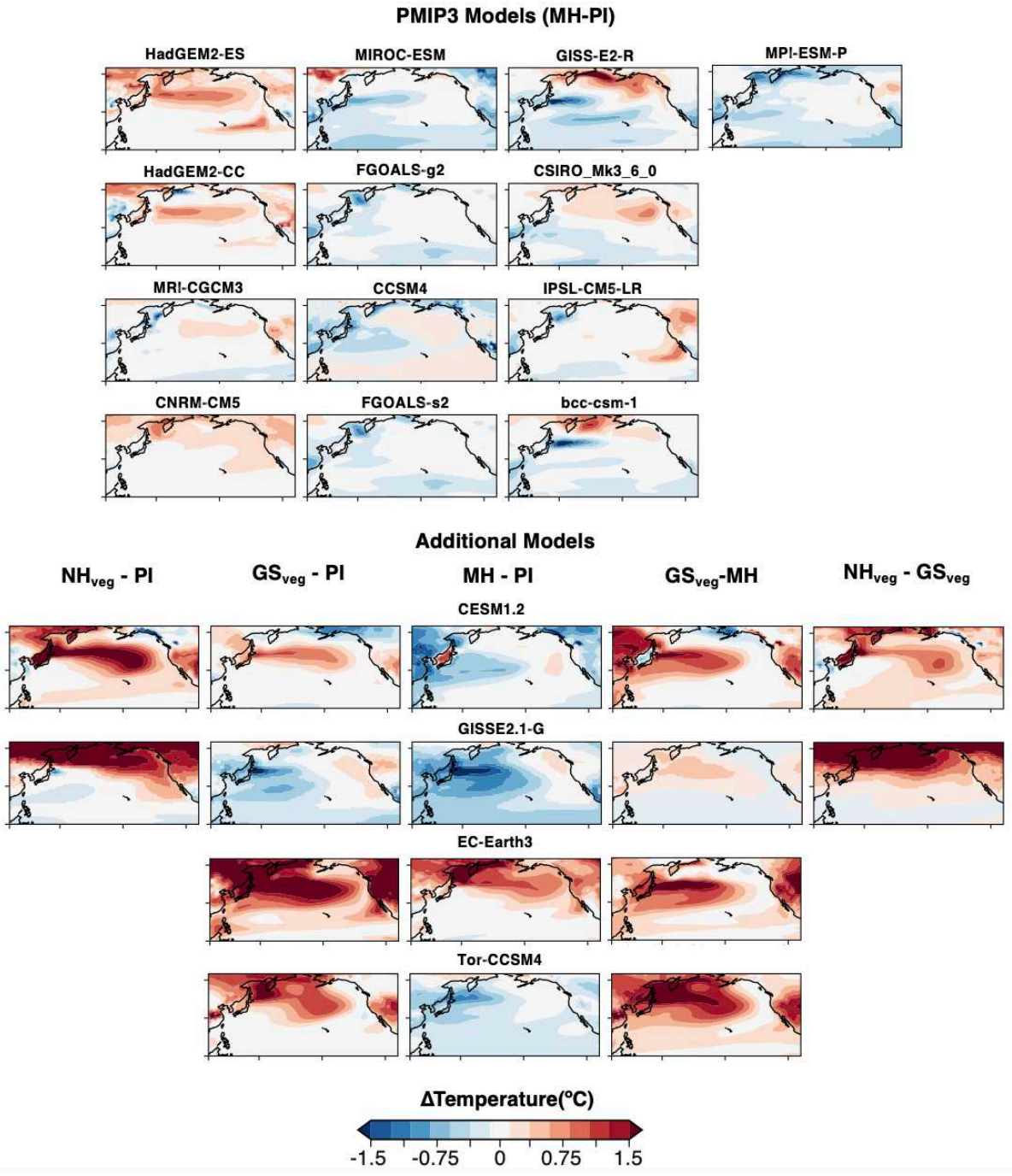

Extended Data Fig. 2.

Mid-Holocene annual sea surface temperature anomalies for the ensemble of the models used in this study. Anomalies computed as MH (6ka)- PI.

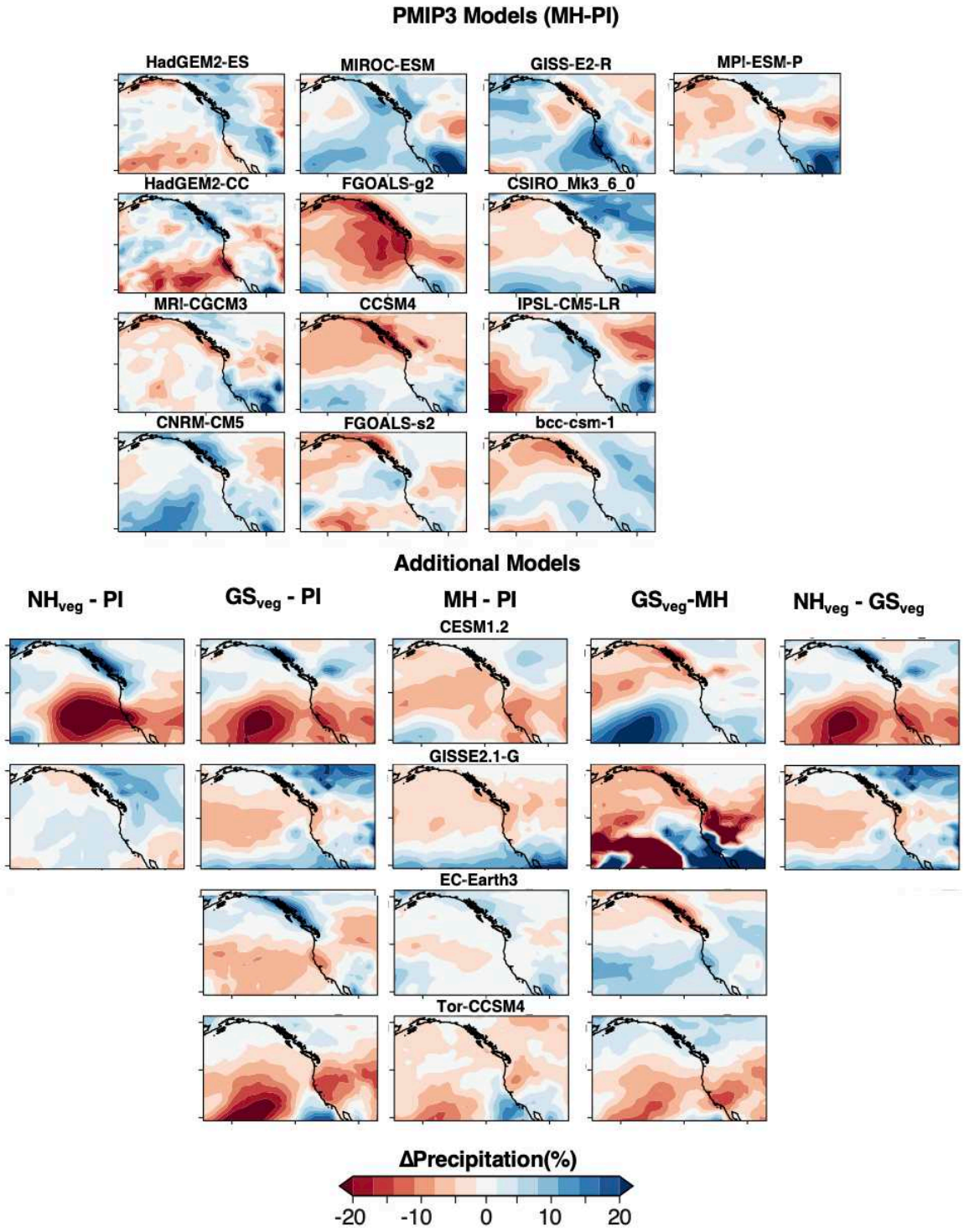

779

780 **Extended Data Fig. 3.**

781 Mid-Holocene annual precipitation anomalies for the ensemble of the models used in this study.
782 Anomalies computed as MH (6ka)- PI.

783

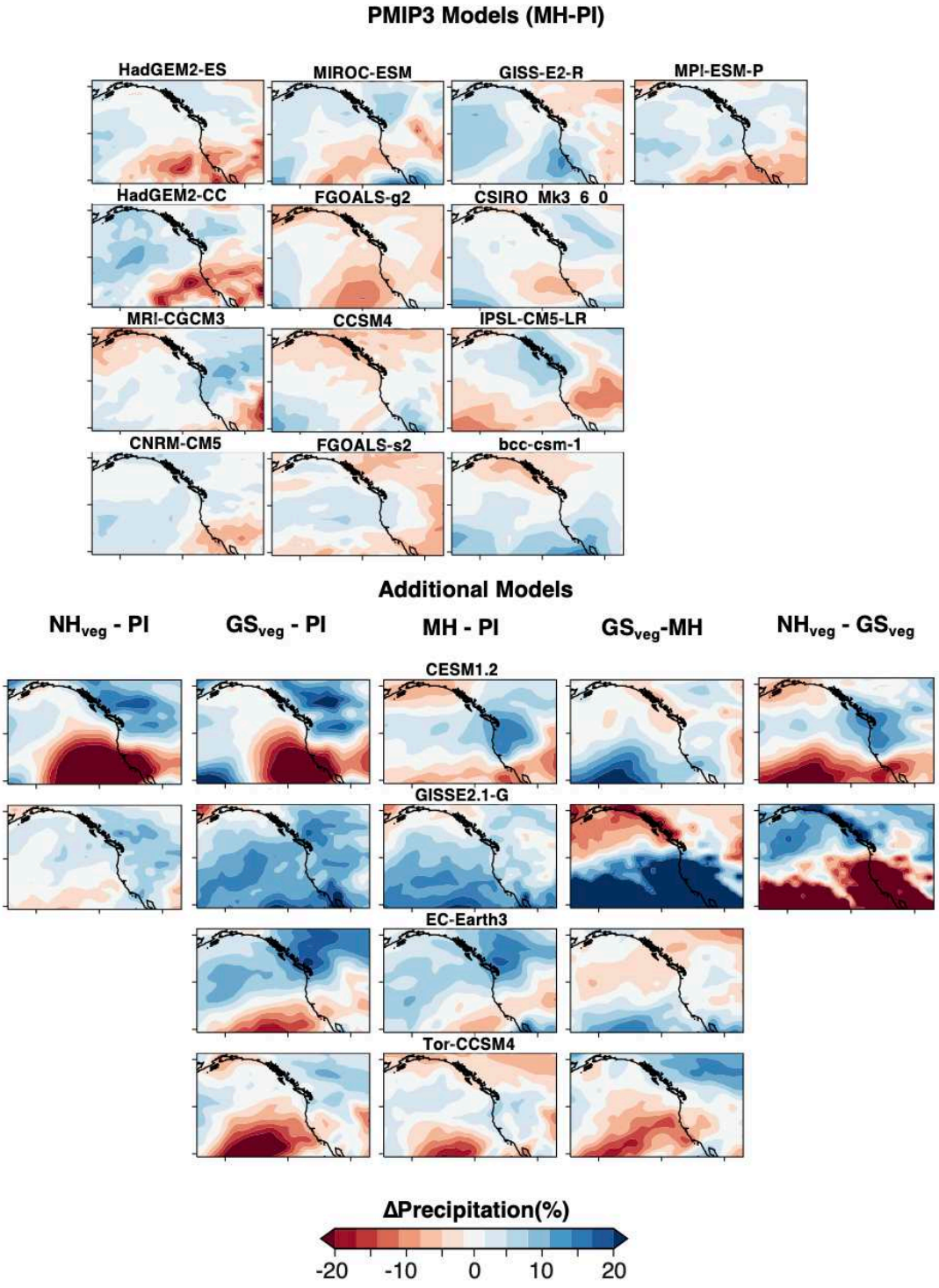

784 **Extended Data Fig. 4.**

785 Mid-Holocene DJF precipitation anomalies for the ensemble of the models used in this study.
786 Anomalies computed as MH (6ka)- PI.

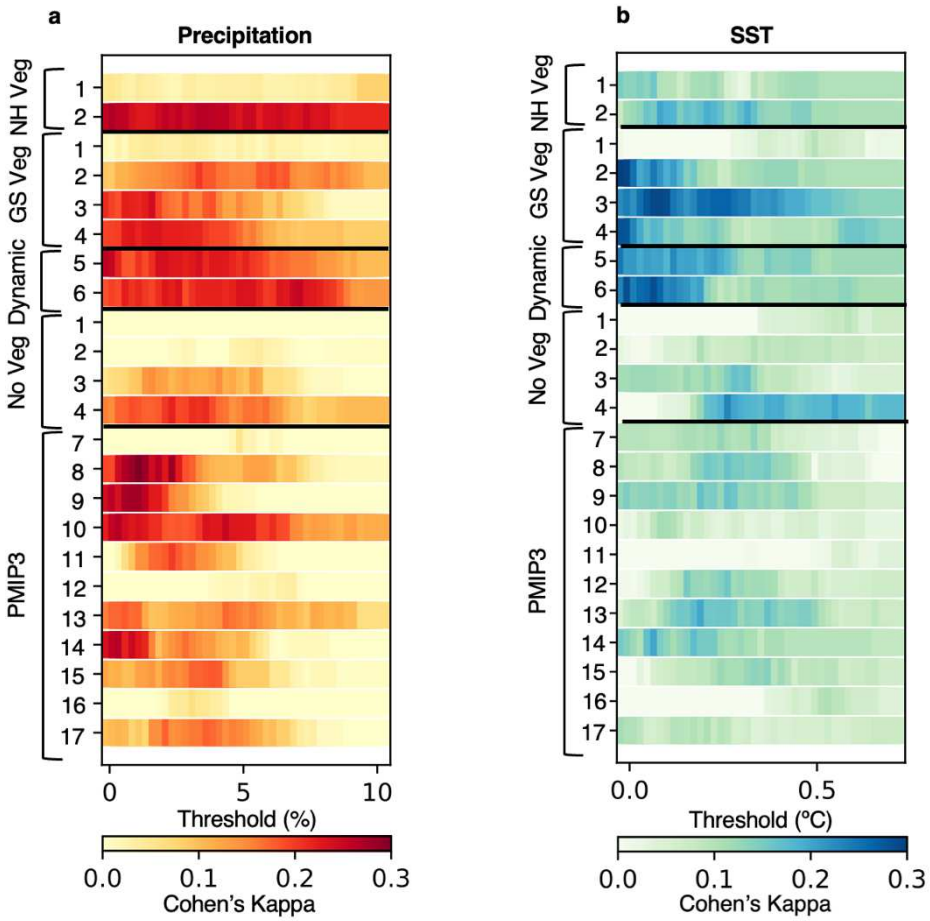

Extended Data Fig. 5.

Cohen's κ for the models as a function of **a.** wetter/drier and **b.** warmer/colder thresholds. Greater agreement is evident in the majority of the models with dynamic or prescribed vegetation. The numbers refer to the following models:
1-GISS-E2-G, 2-CESM1.2, 3-Toronto-CCSM4, 4-EC-Earth, 5-HadGEM2-ES, 6-HadGEM2-CC, 7-CCSM4,8-MPI-ESM-P, 9-IPSL, 10-CSIRO-Mk3, 11-Fgoals-g2, 12-bcc-csm-1, 13-CGCM3, 14-CNRM-CM5, 15-MIROC-ESM, 16- GISS-E2-R, 17-Fgoals-s2.

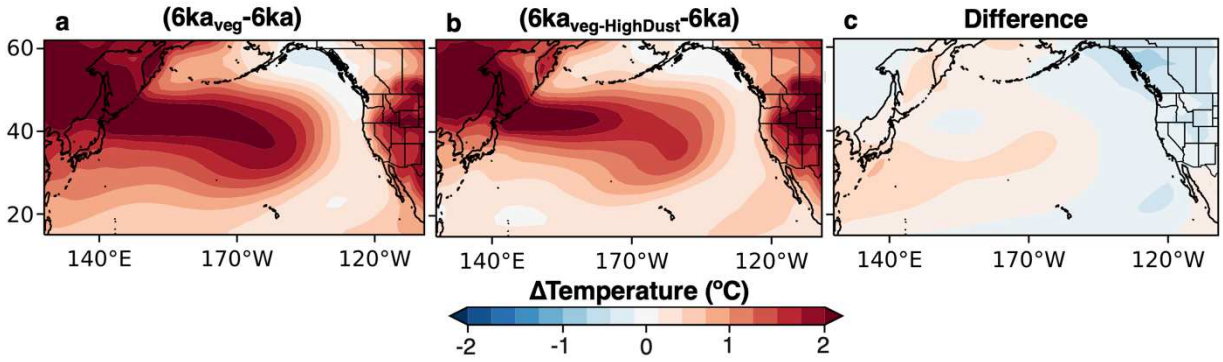

Extended Data Fig. 6.

The role of dust emissions in driving the North Pacific sea surface temperature (SST) patterns in CESM1.2 *(15)*. **a.** The SST anomaly between the simulation with full and no Northern Hemisphere vegetation changes. **b.** The SST anomaly between the simulation with full Northern Hemisphere vegetation changes run with pre-industrial dust emissions (High Dust) and no Northern Hemisphere vegetation changes. **c.** The difference between **a** and **b**.

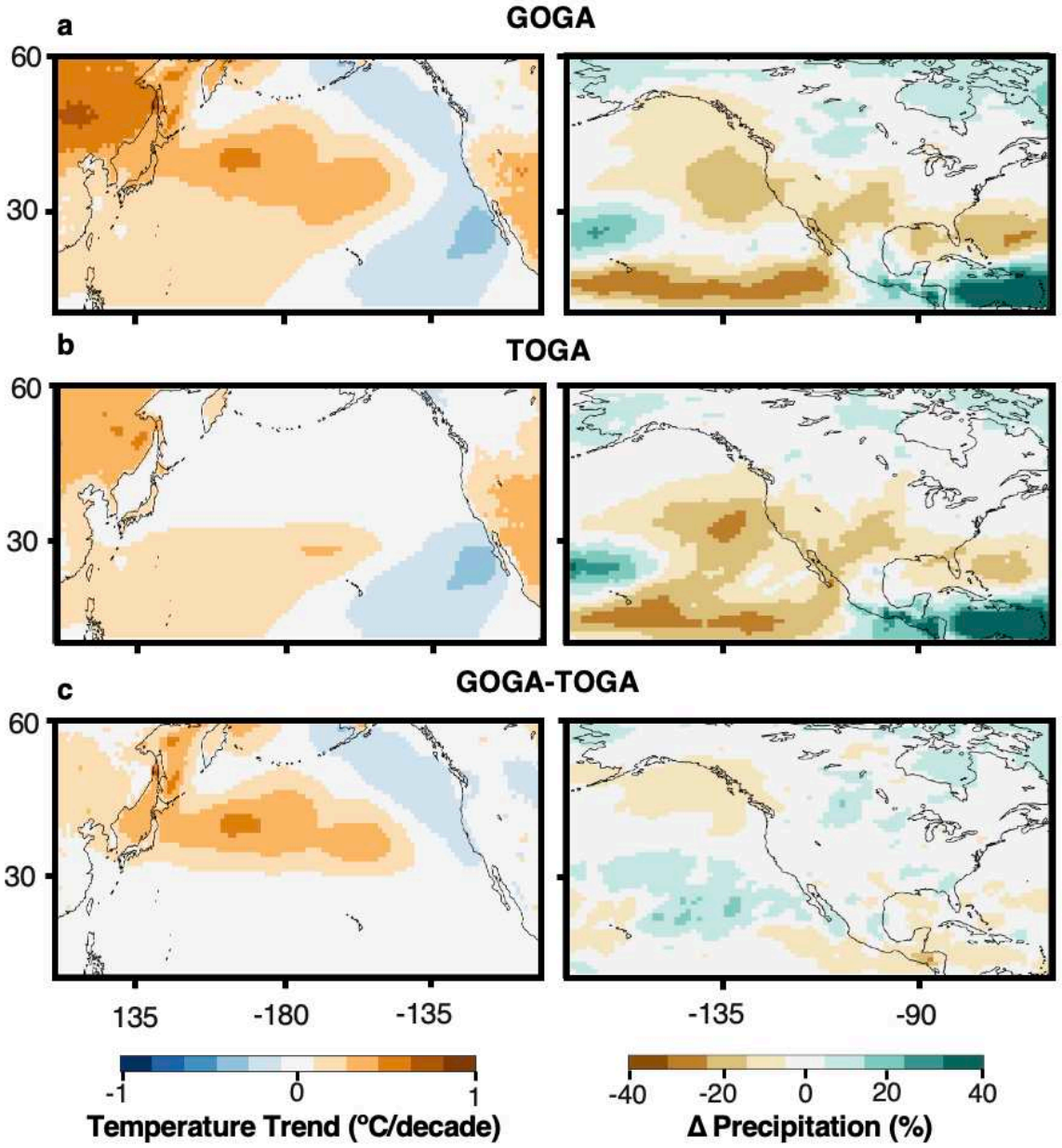

Extended Data Fig. 7.

Temperature trends (°C/decade) and precipitation changes (%) from 1983 to 2019 in the simulations from the **a)** Global Ocean Global Atmosphere (GOGA) and **b)** Tropical Ocean Global Atmosphere (TOGA) simulations as in (*2*). **c)** The difference between the GOGA and TOGA experiments. The GOGA and TOGA simulations were completed by the NCAR Climate Variability and Change Working Group. This data is available from the NCAR Climate Data Gateway.

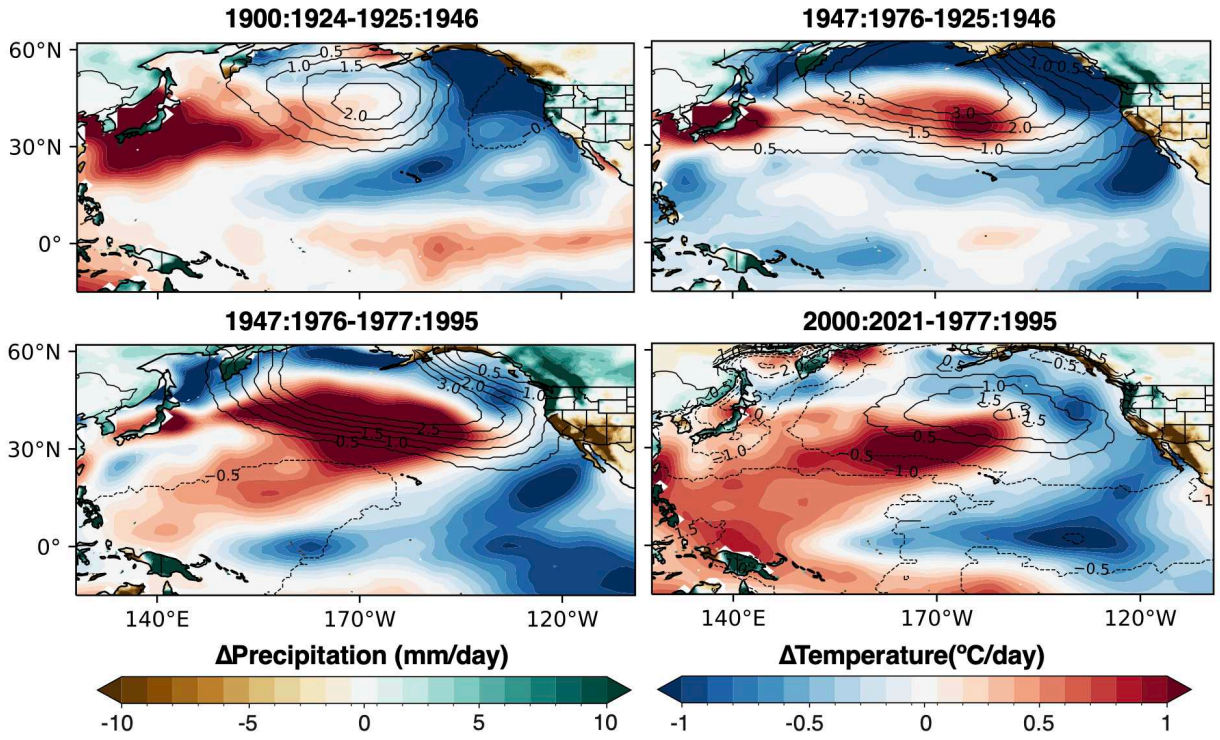

Extended Data Fig. 8.

Modified from ref.[35]. Differences in winter precipitation[37], temperature[51], and sea level pressure[52] between epochs with negative and positive Pacific Decadal Oscillation (PDO) index values. Data provided by the NOAA PSL, Boulder, Colorado, USA, from their website at https://psl.noaa.gov.

Extended Data Table 1.

Summary of the ensemble of mid-Holocene (6 ka) climate model simulations used in this study. The prescribed or fixed vegetation was the same as pre-industrial (PI), included a green Sahara only (GS), or included a Green Sahara and Northern Hemisphere vegetation changes (GS+NH). Mid-Holocene winter (DJF) precipitation change (%) from Pre-industrial for the ensemble of models in the Southwest US (-115°W,-105°W,35°N,40°N).

Model	Vegetation	Atmosphere Resolution	Ocean Resolution	Reference	ΔWinter Precipitation (%)
PMIP 3 Models					
bcc-csm1-1	Prescribed(PI)	2.8×2.8	360 × 232	Wu et al., 2013	4
CCSM4	Prescribed(PI)	0.9×1.25	320 × 384	Gent et al., 2011	-2.1
CNRM-CM5	Fixed (PI)	1.4×1.4	362 × 292	Voldoire et al., 2012	-6.1
CSIRO-Mk3-6-0	Prescribed(PI)	1.9×1.49	192 × 192	Collier et al., 2011	-5.3
FGOALS-g2	Prescribed(PI)	2.813×2.813	360 × 196	Li et al., 2013	-3.7
FGOALS-s2	Prescribed(PI)	2.5x1.666	360 × 196	Bao et al., 2013	-8.2
GISS-E2-R	Fixed (PI)	2×2.5	288 × 180	Russell et al., 1995; Schmidt et al., 2006	-3.6
HadGEM2-CC	Dynamical	1.875×1.25	360 × 216	Bellouin et al., 2007; Collins et al., 2008	-11.1
HadGEM2-ES	Dynamical	1.875×1.25	360 × 216	Bellouin et al., 2007; Collins et al., 2008	-10.6
IPSL-CM5A-LR	Prescribed(PI)	1.875×3.75	182 × 149	Dufresne et al., 2013	-2.2
MIROC-ESM	Prescribed(PI)	128×64	256 × 192	Sueyoshi et al., 2013	-6.5
MPI-ESM-P	Fixed (PI)	1.9×1.9	256 × 220	Giorgetta et al., 2012	-6.9
MRI-CGCM3	Prescribed(PI)	320×160	364 × 368	Yukimoto et al., 2012	-10.4
Additional Models					
CESM1.2	Fixed (PI)	1.9×2.5	360×180	Thompson et al., 2022	-1.1
CESM1.2_NHveg	Fixed(Full NH vegetation)	1.9×2.5	360×180	Thompson et al., 2022	-14
CESM1.2_GS	Fixed (Green Sahara)	1.9×2.5	360×180	Tabor et al., 2020	-12.8
UofT-CCSM4	Fixed (PI)	1x1	360×180	Chandan and Peltier, 2020	-5.2
UofT-CCSM4_GS	Fixed (Green Sahara)	1x1	360×180	Chandan and Peltier, 2020	-7
EC-Earth3.1	Fixed (PI)	1.125x1.125	360×180	Pausata et al., 2016	-5.2
EC-Earth3.1_GS	Fixed (Green Sahara)	1.125x1.125	360×180	Pausata et al., 2016	-6.6
GISS-E2-G	Fixed (PI)	2x2.5	360x144	Tiwari et al., 2023	4.5
GISS-E2-G_GS	Fixed (Green Sahara)	2x2.5	360x145	Tiwari et al., 2023	2.3
GISS-E2-G_NHveg	Fixed(Full NH vegetation)	2x2.5	360x146	Tiwari et al., 2023	0.2

Extended Data Table 2.

Summary of the synthesized proxy precipitation and sea surface temperature records used in this study. Dry = -1, Wet = +1, 0=unchanged.

	Site	Latitude	Longitude	Change (+1,-1,0)	Proxy	References
1	Laguna Seca San Felipe	31.13	-115.25	-1	Lake Sediment	Roy et al 2010
2	Cave of the Bells	31.43	-110.47	-1	Speleothem	Wagner 2006
3	Lake Cloverdale	31.50	-108.83	-1	Lake Sediment	Krider 1998
4	Whitewater Draw	31.66	-109.70	-1	Lake Sediment	LaMarche, 1973
5	Chihuahuan Desert	31.76	-106.48	1	Lake Sediment	Van Devender, 1990
6	Santa Cruz River	31.95	-110.96	-1	Lake Sediment	Waters, 2001
7	San Pedro Valley	32.00	-110.30	-1	terrestrial sediment	Pigati et al., 2009
8	San Pedro River	32.03	-110.31	-1	Lake Sediment	Waters, 2001
9	Pink Panther Cave	32.08	-105.17	1	d18O	Asmerom et al 2007
10	Willcox Playa/Lake Cochise	32.13	-109.85	-1	Lake Sediment	Waters, 1989
11	Guadalupe Mountains	32.15	-104.56	-1	speleothem	Polyak and Asmerom, 2001
12	Lake Lucero Playa	32.71	-106.44	-1	dune	Langford 2003
13	Dry Lake	34.12	-116.83	-1	Charcoal, microfossil, grain size, MS, LOI; GPR	Bird and Kirby 2006; Bird et al., 2009
14	Lower Bear Lake	34.14	-116.58	-1	CN	Kirby et al 2012
15	Santa Barbara Basin	34.28	-120.04	-1	Lake Sediment	Du et al., 2017
16	Lake Estancia	34.65	-105.95	-1	morphology, Stratigraphy, brine shrimp cysts	Anderson et al 2000, Menking, 2004; Menking and Anderson 2003, Allen and Anderson 2000
17	Mojave Desert	35.00	-117.00	1	Alluvial fan dates	Miller et al. 2010
18	Cavenee Cave	35.08	-106.13	-1	Speleothem	Polyak and Asmerom, 2005
19	Silver Lake	35.34	-116.11	-1	MS, grain size, C:N, TN, TOC, LOI, ostracodes	Kirby et al., 2015
20	China Lake	35.74	-117.62	-1	Lake Sediment	Rosenthal et al., 2017
21	Chihuahuenos Bog	36.02	-106.30	-1	pollen, d13C, lake level	Cisneros-Dozal et al 2010, Anderson et al., 2008
22	Ash Meadows	36.41	-116.32	1	Lake Sediment	Mehringer and Warren, 1976

23	Owens Lake	36.42	-117.88	-1	lake level	Bacon et al 2006, 2013, 2020; Benson et al 1996; Mensing 2001
24	Devils Hole	36.43	-116.29	-1	d18O	Winograd et al 2006; Moseley et al 2016
25	Crane Lake	36.53	-112.15	1	pollen transfer function	Herzschuh et al., 2022
26	Las Vegas Valley	36.56	-115.51	-1	black mat, d13C	Quade et al 1998
27	Lilypad Lake	36.98	-118.99	-1	pollen transfer function	Herzschuh et al., 2022
28	Cumbres Bog	37.02	-106.45	-1	pollen transfer function	Herzschuh et al., 2022
29	Balsam Meadows	37.17	-119.50	-1	Pollen, macrofossils, charcoal	Davis et al 1985
30	Lower Pahranagat Lake	37.22	-115.09	1	d18O, d13C	Theissen et al 2019
31	Nichols Meadow	37.42	-119.58	-1	pollen transfer function	Herzschuh et al., 2022
32	Clear Lake	37.49	-107.47	-1	dust	Arcusa et al 2020
33	Lake Barrett	37.60	-119.01	-1	Diatom; MS, lake level	MacDonald et al 2008; Anderson et al., 1990
34	Starkweather Pond	37.67	-119.07	1	lake level	Anderson et al., 1990
35	White Mountains	37.70	-118.33	0	dD	Jennings and Elliot-Fisk 1993
36	Little Molas Lake	37.74	-107.71	-1	lake level	Shuman et al 2015
37	Siesta Lake	37.85	-119.66	-1	pollen transfer function	Brunelle and Anderson 2003
38	Leviathan Cave	37.89	-115.58	-1	d18O	Lachniet et al 2014
39	Lake Emma	37.90	-107.62	-1	pollen transfer function	Herzschuh et al., 2022
40	Sierra Nevada	37.91	-119.26	-1	Terrestrial Sediment	Anderson and Smith, 1994
41	Lake Kirman	38.20	-119.30	-1	lake level	McDonald et al 2016
42	Hidden Lake	38.26	-119.52	-1	lake level	Potito et al., 2006
43	Kirman Lake	38.33	-119.50	-1	LOI, CN, Diatoms	MacDonald et al., 2016
44	Sevier Lake	38.95	-113.14	-1	lake level	Oviatt, 1988
45	Lehman Cave	39.01	-114.22	-1	Speleothem	Steponaitis et al 2015
46	Lake Tahoe	39.10	-120.03	-1	Lake Sediment	Lindstrom, 1990
47	McMurray Lake	39.46	-120.65	-1	pollen transfer function	Herzschuh et al., 2022
48	Yellow Lake	39.65	-107.35	-1	d18O	Anderson, 2011
49	Grassy Lake	39.70	-120.66	-1	pollen transfer function	Herzschuh et al., 2022
50	Bison Lake	39.77	-107.35	-1	d18O	Anderson, 2011
51	Stonehouse Meadow	39.78	-114.54	-1	Lake Sediment	Mensing et al., 2013
52	Humboldt Sink	40.04	-118.45	-1	Lake Sediment	Byrne et al., 1979

53	Favre Lake	40.34	-115.23	-1	pollen, charcoal, grain size	Wahl et al 2015
54	Blue Lake Wetlands	40.50	-114.03	-1	pollen transfer function	Herzschuh et al., 2022
55	CA-HUM-558 (Pilot Ridge)	40.66	-123.67	-1	pollen transfer function	Herzschuh et al., 2022
56	Upper Big Creek Lake	40.91	-106.62	-1	lake level	Shuman et al., 2015
57	Marsh Lake Bog	40.98	-110.40	-1	pollen, CaCO3%	Louderback et al., 2015
58	Camp Bog	41.00	-110.38	-1	pollen, CaCO3%	Louderback et al., 2015
59	Flycatcher Basin	41.02	-121.57	-1	pollen transfer function	Herzschuh et al., 2022
60	Great Salt Lake	41.11	-112.53	-1	Lake Sediment	Spencer et al., 1984
61	Homestead Cave	41.16	-112.93	-1	lake level	Madsen et al., 2001
62	Little Windy Hill pond	41.43	-106.33	-1	lake level	Pribyl and Shuman, 2014
63	Grass Lake	41.65	-122.17	-1	pollen transfer function	Herzschuh et al., 2022
64	Bear Lake	42.00	-111.33	-1	lake level	Doner et al., 2009
65	Bolan Lake	42.02	-123.46	-1	LOI, MS, charcoal, pollen	Briles et al 2005
66	Minnetonka Cave	42.09	-111.52	0	d18O	Lundeen et al 2013
67	Oregon Caves Nat. Mon.	42.10	-123.41	0	d18O	Ersek et al 2012
68	paleo-Lake Malheur	43.34	-118.76	-1	lake level	Dugas 1998
69	Lake of the Woods	43.48	-109.89	-1	stratigraphy	licciardi et al 2004; Shuman et al 2009; Shuman and Serravezza 2017
70	Tumalo Lake	44.02	-121.54	-1	pollen transfer function	Herzschuh et al., 2022
71	Emerald Lake	44.07	-110.30	1	pollen transfer function	Herzschuh et al., 2022
72	South Fork Payette River	44.07	-115.51	1	other	Pierce et al., 2004
73	Duncan Lake	44.65	-107.45	-1	lake level	Shuman and Serravezza, 2017
74	Slough Creek Pond	44.93	-110.35	-1	pollen transfer function	Herzschuh et al., 2022
75	Crevice Lake	45.00	-110.58	1	d18O	Whitlock, 2012
76	Dailey Lake	45.26	-110.82	1	pollen transfer function	Herzschuh et al., 2022
77	Hoodoo Lake	46.32	-114.65	1	pollen transfer function	Herzschuh et al., 2022
78	Star Meadows	46.52	-114.68	1	pollen, CaCO3, ms	Herring and Gavin 2015

79	Jay Bath	46.77	-121.77	-1	Pollen, charcoal, macrofossils	Dunwiddie 1986
80	Reflection Pond	46.77	-121.73	-1	Pollen, charcoal, macrofossils	Dunwiddie 1986
81	Log Wallow	46.78	-121.75	-1	Pollen, charcoal, macrofossils	Dunwiddie 1986
82	Jones Lake	47.05	-113.14	-1	d18O, d13C, Aragnite:calcite, ms, ARM/IRM	Shapley et al 2009; Maxbauer et al 2020
83	Lost Lake	47.64	-110.48	-1	pollen transfer function	Herzschuh et al., 2022
84	Martins Lake	47.71	-123.53	1	pollen transfer function	Herzschuh et al., 2022
85	Moose Lake	47.88	-123.35	1	pollen transfer function	Herzschuh et al., 2022
86	Crocker Lake	47.94	-122.88	0	pollen transfer function	Herzschuh et al., 2022
87	Wentworth Lake	48.01	-124.53	1	pollen transfer function	Herzschuh et al., 2022
88	Foy Lake, Montana	48.17	-114.35	-1	lake level	Shuman et al 2009, Power et al., 2005
89	Kirk Lake	48.23	-121.62	1	pollen transfer function	Herzschuh et al., 2022
90	Langford Lake	48.45	-123.53	0	pollen transfer function	Brown et al 2006
91	Heal Lake	48.53	-123.47	0	pollen transfer function	Brown et al 2006
92	Walker Lake	48.53	-124.00	1	pollen transfer function	Herzschuh et al., 2022
93	Castor Lake	48.54	-119.56	-1	d18O, d13C	Steinman et al 2019
94	Scanlon Lake	48.54	-119.58	-1	CaCO3%	Steinman et al 2019
95	Begbie Lake	48.59	-123.68	0	pollen transfer function	Herzschuh et al., 2022
96	Killebrew Lake Fen	48.61	-122.90	1	pollen transfer function	Herzschuh et al., 2022
97	Rhamnus Lake	48.63	-123.72	0	pollen transfer function	Brown et al 2006
98	Panther Potholes	48.66	-121.04	-1	pollen transfer function	Herzschuh et al., 2022
99	Whyac Lake Bog	48.67	-124.84	0	pollen transfer function	Brown et al 2006
100	Swiftcurrent Lake	48.80	-113.66	1	grain size, C/N, ms	MacGregor et al 2011
101	Effingham Island Bog	48.87	-125.32	0	pollen transfer function	Brown et al 2006
102	Lime Lake	48.87	-117.34	1	d18O	Steinman et al 2016
103	Boomerang Lake	49.18	-124.16	-1	pollen transfer function	Brown et al 2006
104	Enos Lake	49.28	-124.16	0	pollen transfer function	Brown et al 2006
105	Marion Lake	49.31	-122.55	1	pollen transfer function	Herzschuh et al., 2022
106	Turtle Lake	49.33	-124.96	0	pollen transfer function	Brown et al 2006

107	Cooley Lake	49.49	-117.65	-1	pollen transfer function	Herzschuh et al., 2022
108	Harris Lake	49.67	-109.90	-1	pollen transfer function	Herzschuh et al., 2022
109	Grant's Bog	49.79	-125.13	1	pollen transfer function	Herzschuh et al., 2022
110	Arch Cave, Canada	50.55	-127.10	1	d18O	Marshall et al 2009
111	Dog Lake	50.78	-115.93	1	Lake Sediment	Hallett and Hills 2006
112	Cleland Lake	50.83	-116.39	1	d18O	Steinman et al 2016
113	Woods Lake	51.00	-127.27	1	pollen transfer function	Herzschuh et al., 2022
114	Two Frog Lake	51.11	-127.53	1	pollen transfer function	Herzschuh et al., 2022
115	Felker Lake	51.57	-121.60	1	diatom-based Salinity, Lake depth	Galloway et al 2011
116	Louise Pond	52.95	-131.76	-1	pollen transfer function	Herzschuh et al., 2022
117	Morkill Lake	53.61	-120.65	-1	pollen transfer function	Herzschuh et al., 2022
118	Gerry Lake	53.65	-121.51	-1	pollen transfer function	Herzschuh et al., 2022
119	SC1 Pond	54.42	-131.91	-1	pollen transfer function	Herzschuh et al., 2022
120	Paradise Lake	54.69	-122.62	1	d18O	Steinman et al 2016
121	Berendon Fen	56.24	-130.06	-1	pollen transfer function	Herzschuh et al., 2022
122	Hummingbird Lake	56.55	-135.01	1	pollen transfer function	Herzschuh et al., 2022
123	Rasberry Bog	57.48	-130.83	1	pollen transfer function	Herzschuh et al., 2022
124	Skinny Lake	57.59	-130.10	0	pollen transfer function	Herzschuh et al., 2022
125	Sunset Lake	58.50	-124.65	-1	pollen transfer function	Herzschuh et al., 2022
126	Lily Lake	59.20	-135.40	1	pollen transfer function	Herzschuh et al., 2022
127	Lac Ciel Blanc	59.52	-122.17	-1	pollen transfer function	Herzschuh et al., 2022
128	Choquette Lake	59.95	-151.11	0	pollen transfer function	Herzschuh et al., 2022
129	Hail Lake	60.03	-129.02	-1	pollen transfer function	Herzschuh et al., 2022
130	Munday Creek	60.03	-141.97	-1	pollen transfer function	Herzschuh et al., 2022
131	Marcella Lake	60.07	-133.81	-1	pollen transfer function	Herzschuh et al., 2022
133	Goat Lake	60.26	-149.91	-1	pollen transfer function	Herzschuh et al., 2022
134	Jellybean Lake	60.35	-134.80	-1	carbonate d18O	Barron et al., 2010
135	Jigsaw Lake	60.44	-150.30	-1	Lake Sediment	Berg et al., 2022

136	Salmo Lake	60.45	-133.56	-1	pollen transfer function	Herzschuh et al., 2022
137	Mt.Logan	60.57	-140.41	-1	ice core d18O	Barron et al., 2010
138	Snipe Lake	60.63	-154.30	0	pollen transfer function	Herzschuh et al., 2022
139	Mica Lake	60.69	-148.14	-1	pollen transfer function	Herzschuh et al., 2022
140	Dolly Varden Lake site B1	60.71	-150.79	-1	Lake Sediment	Berg et al., 2022
141	Dragonfly Lake	60.81	-135.34	-1	pollen transfer function	Herzschuh et al., 2022
	Site	Lat	Lon	ΔT (ºC)	Proxy	References
1	MD032601	-66.00	138.60	0.718	tex86	Crosta et al., 2007
2	ODP_178_1098B	-64.86	-64.21	0.064	tex86	Shevenell et al., 2011
3	JPC67	-54.32	-69.46	-0.594	uk37	Bertrand et al., 2017
4	Churruca	-53.03	-73.90	0.676	uk37	Caniupan et al., 2014
5	MD07-3124	-50.52	-74.97	0.020	uk37	Caniupan et al., 2014
6	JPC42	-49.92	-74.38	0.329	uk37	Caniupan et al., 2014
7	MD07-3088	-46.07	-75.68	-0.128	pollen	Montade et al., 2019
8	md97-2120	-45.53	174.93	-0.172	uk37	Pahnke et al., 2003
9	SO136_GC11	-43.44	167.85	1.122	uk37	Barrows et al., 2007
10	GeoB33131	-41.00	-74.30	0.241	uk37	Lamy et al., 2002
11	md97-2121	-40.38	177.99	0.604	uk37	Pahnke and Sachs, 2006
12	rr0503-87tc	-37.26	176.66	0.050	uk37	Sikes et al., 2019
13	MD03_2607-Assemblage	-36.96	137.41	1.190	uk37	Lopes dos Santos et al., 2013
14	MD03_2611	-36.73	136.55	-0.749	d18O	Calvo et al., 2007
15	GIK17748-2	-32.75	-72.03	2.430	uk37	Kim et al., 2002
16	geob7139-2	-30.20	-71.98	1.201	uk37	Kaiser et al., 2008
17	M135_005_3	-17.42	-71.77	-0.594	uk37	Salvatteci et al., 2019
18	M135_004_3	-17.41	-71.74	-0.511	uk37	Salvatteci et al., 2019
19	M77_2_003_2	-15.10	-75.69	-0.936	uk37	Salvatteci et al., 2019
20	M77_2_024_5	-11.08	-78.02	-0.657	uk37	Salvatteci et al., 2019
21	MD98_2165	-9.65	118.40	0.154	mgca	Levi et al., 2007
22	M77_2_029_3	-9.30	-79.62	0.989	uk37	Salvatteci et al., 2019
23	GeoB10069_3	-9.01	120.02	1.193	mgca	Gibbons et al., 2014
24	GeoB10053_7	-8.68	112.87	-0.874	d18O	Mohtadi et al., 2010
25	BJ8_03_10GGC	-7.37	115.25	0.490	d18O	Linsley et al., 2010
26	geob10043-3	-7.31	105.06	0.016	mgca	Setiawan et al., 2015
27	gik18540-3	-6.87	119.58	-0.415	mgca	Schroder et al., 2018
28	MD98_2161	-5.21	117.48	0.837	mgca	Fan et al., 2018
29	MD98_2176	-5.00	133.44	0.866	mgca	Stott et al., 2007
30	md98-2162	-4.70	117.90	0.422	mgca	Visser et al., 2003

31	RR1313_23 PC	-4.49	145.67	0.498	mgca	Moffa-Sanchez et al., 2019
32	KNR195_5_ CDH26	-3.99	-81.31	0.318	uk37	Bova et al., 2015
33	m77-2-059-1	-3.95	-81.32	0.481	uk37	Nurnberg et al., 2015
34	M77_2_056 _5	-3.75	-81.12	1.183	mgca	Nurnberg et al., 2015
35	GiK18515_3	-3.63	119.36	1.039	mgca	Schroder et al., 2010
36	gik18526-3	-3.61	118.17	0.134	mgca	Schroder et al., 2018
37	BJ8_03_70G GC	-3.57	119.38	0.809	mgca	Linsley et al., 2010
38	geob17419-1	-2.81	144.50	0.834	mgca	Hollstein et al., 2018
39	ERDC_092 BX	-2.23	157.00	-0.944	d18O	Palmer et al., 2003
40	me0005a-27jc	-1.85	-82.79	-0.085	uk37	Dubois et al., 2009
41	geob10029-4	-1.49	100.13	-0.048	mgca	Mohtadi et al., 2010
42	SO189_039 KL	-0.79	99.91	-0.303	mgca	Mohtadi et al., 2014
43	gik18519-2	-0.57	118.11	0.430	mgca	Schroder et al., 2018
44	me0005a-24jc	0.02	-86.46	-0.924	uk37	Kienast et al., 2006
45	SO189_144 KL	1.16	98.07	0.122	d18O	Mohtadi et al., 2014
46	gik18522-3	1.40	119.08	0.195	mgca	Schroder et al., 2018
47	SO189_119 KL	3.52	96.32	-0.451	mgca	Mohtadi et al., 2014
48	md98-2178	3.62	118.70	0.432	mgca	Fan et al., 2018
49	MD97_2151	8.73	109.87	0.354	tex86	Yamamoto et al., 2013
50	PL07_39PC	10.70	-65.94	-0.789	d18O	Lea et al., 2003
51	odp165-1002c	10.71	-65.17	-0.053	uk37	Herbert and Schuffert, 2000
52	VM12_107	11.33	-66.63	-0.835	mgca	Schmidt et al., 2012
53	m35003-4	12.09	-61.24	-0.372	uk37	Ruhlemann et al., 1999
54	so164-03-4	16.54	-72.21	0.616	mgca	Reissig et al., 2018
55	gik17286-1	19.74	89.88	-0.497	uk37	Lauterbach et al., 2020
56	odp_184-1144_2	20.05	117.42	-0.230	mgca	Moffa-Sanchez et al., 2019
57	so204b	21.23	118.05	0.101	mgca	Yang et al., 2019
58	yj	21.52	112.13	1.285	uk37	Zhang et al., 2019
59	ori715-21	22.70	121.50	-0.639	mgca	Lo et al., 2013
60	RC12-10	23.00	-95.53	1.792	diatoms	Poore et al., 2003
61	KNR166_JP C51	24.41	-83.22	0.913	mgca	Schmidt et al., 2012
62	mv99-pc14	25.20	-112.72	-0.951	mgca	Marchitto et al., 2010
63	KNR159_JP C26	26.37	-92.03	2.565	mgca	Antonarakou et al., 2015
64	A7	27.82	126.98	-0.712	d18O	Sun et al., 2005
65	MD02_2575 BAY	29.00	-87.12	2.263	mgca	Ziegler et al., 2008
66	KY07_04_P C1	31.63	128.95	0.546	mgca	Kubota et al., 2010
67	kt92-17_st14	31.90	137.80	0.068	uk37	Sawada and Handa, 1998
68	893A	34.29	-120.04	1.271	d18O	Kennett et al., 2007

69	MD02_2503	34.39	-120.04	0.284	d18O	Sarnthein et al., 2014
70	SSDP_102	34.95	128.88	-0.611	uk37	Kim et al., 2004
71	MD01_2421	36.03	141.78	1.112	d18O	Isono et al., 2009
72	ch07-98_ggc19	36.87	-74.57	2.324	uk37	Sachs, 2007
73	station_6_mc	37.75	162.43	-0.182	uk37	Harada et al., 2004
74	station_5_mc	40.00	165.07	1.894	uk37	Harada et al., 2004
75	PC6	40.40	143.50	0.789	uk37	Minoshima et al., 2007
76	kt05-7-pc02	41.00	140.77	0.265	uk37	Kawahata et al., 2009
77	ODP_167_1019C	41.68	-124.93	-1.174	uk37	Barron et al., 2003
78	w8709a-8tc	42.24	-127.68	-0.667	uk37	Prahl et al., 1995
79	OCE326_GGC30	43.89	-62.80	4.014	uk37	Sachs, 2007
80	MD01_2412	44.53	145.00	-1.211	uk37	Harada et al., 2006
81	MR003-K03-PC01	46.32	152.53	0.507	uk37	Harada et al., 2004
82	jt96-09	48.90	-126.88	-0.073	uk37	Kienast and McKay, 2001
83	pc04	49.37	153.02	0.395	uk37	Harada et al., 2004
84	2005-804-006	68.99	-106.57	0.492	diatoms	Ledu et al., 2010
85	GGC19	72.16	-155.51	0.219	d18O	Farmer et al., 2011
86	HLY0501	72.69	-157.52	0.454	diatoms	de Vernal et al., 2013
87	P1B3	73.68	-162.66	0.596	diatoms	de Vernal et al., 2005
88	HU91-039-008	77.27	-74.33	1.565	diatoms	Levac et al., 2001

831
832

833